WILEY

RESEARCH ARTICLE

Modeling the mechanics of axonal fiber tracts using the embedded finite element method

Harsha T. Garimella [1] | Reuben H. Kraft [1,2]

[1]Department of Mechanical and Nuclear Engineering, The Pennsylvania State University, University Park, PA 16802, USA

[2]Department of Biomedical Engineering, The Pennsylvania State University, University Park, PA 16802, USA

Correspondence
Reuben Kraft, Department of Mechanical and Nuclear Engineering, The Pennsylvania State University, University Park, PA, USA.
Email: reuben.kraft@psu.edu

Abstract

A subject-specific human head finite element model with embedded axonal fiber tractography obtained from diffusion tensor imaging was developed. The axonal fiber tractography finite element model was coupled with the volumetric elements in the head model using the embedded element method. This technique enables the calculation of axonal strains and real-time tracking of the mechanical response of the axonal fiber tracts. The coupled model was then verified using pressure and relative displacement-based (between skull and brain) experimental studies and was employed to analyze a head impact, demonstrating the applicability of this method in studying axonal injury. Following this, a comparison study of different injury criteria was performed. This model was used to determine the influence of impact direction on the extent of the axonal injury. The results suggested that the lateral impact loading is more dangerous compared to loading in the sagittal plane, a finding in agreement with previous studies. Through this analysis, we demonstrated the viability of the embedded element method as an alternative numerical approach for studying axonal injury in patient-specific human head models.

KEYWORDS

axonal fiber network, axonal injury, diffusion tensor imaging, embedded element method, finite element model, tractography

1 | INTRODUCTION

Traumatic brain injury is a debilitating injury and a significant health problem in the United States that is estimated to occur in 1.6 to 1.8 million people annually.[1] Axonal injury is a common type of traumatic brain injury primarily characterized by damage to the axons.[2,3] Enhanced knowledge of the axonal deformation during a head impact may facilitate a better understanding of the primary injury mechanism and secondary effects that may lead to functional deficits and long-term neurodegeneration. This information may also enable the development of improved diagnostic tools, protective measures, and rehabilitation treatments.[4] A consensus on the best way to study the axonal injury during the milder forms of traumatic brain injury, such as concussion, is still lacking.[5]

Finite element models might offer a means to numerically study the evolution of axonal injury. Several finite element head models have been developed,[6–25] demonstrating that the constitutive laws, anatomical resolution, and injury descriptions have improved over time. However, there remains a gap in elucidating the relationship between the stress-strain measures obtained from finite element models and the mechanical thresholds for cellular injury. One approach to bridge this gap might be increasing the level of anatomical detail in the finite element models. Over the years, many successful attempts were made at leveraging data associated with medical imaging, including diffusion tensor imaging, to develop higher resolution biofidelic computational head models. In this work, we are particularly interested in leveraging the maximum amount of information from DTI into our model. Table 1 presents a list of finite element studies that have used diffusion tensor imaging in computational models of brain trauma. Most of the studies[4,26–35] listed in Table 1 adopted diffusion tensor imaging to inform anisotropic material models representing brain tissue. In a few studies, anisotropy was implemented in the models using fractional anisotropy

TABLE 1 A list of studies in which diffusion tensor imaging is applied to introduce structural detail into FE element head models

Study	White Matter (WM) Material Model	Algorithm for Mapping of DTI Data to FE model	Major Findings
Chatelin et al [26]	Isotropic, viscoelastic. Fiber directions per element: 1	Image fitting using rigid transformations. Mapped multiple DTI voxels per FE.	Axonal strains were significantly smaller than von Mises strain and the first principal strain.
Ji et al [34]	Isotropic, visco-hyperelastic.	Fiber orientations, calculated on the basis of the primary eigen vector, are then transferred to FE model coordinate system.	Significant differences in predicted WM damage between first principal strain and axonal strain.
Zhao et al [35]	Isotropic, visco-hyperelastic.	Used DTI tractography models directly without any averaging procedures instead of a voxel-based approach.	The coronal rotation of human head resulted in more axonal damage compared to sagittal rotation.
Colgan et al [27]	Anisotropic, hyperelastic. Fiber directions per element: 1	Distinct fiber directions that define each voxel region are averaged. FE elements registered to 3D FA map. Mapped multiple DTI voxels per FE.	Inclusion of anisotropy had a significant effect on the magnitude of developed shear strains.
Wright et al [28]/[29]	Anisotropic, hyperelastic/visco-hyperelastic.	Fiber orientation vectors, calculated from FA maps, were overlapped with their FE model. 2D FE models were used in the analysis.	Degree of white matter injury depends highly on the fiber orientation.
Kraft et al [30]	Anisotropic, hyperelastic. Fiber directions per element: 1	An explicit DTI fiber tractography was used to determine fiber orientation vectors. Mapped multiple fibers per FE by averaging.	Developed a time-evolving strain injury criterion and a physics based injury model.
Sahoo et al [31]	Anisotropic, visco-hyperelastic. Fiber directions per element: 1	Same as that of Chatelin et al[26]	Inclusion of anisotropy had a significant effect on the developed principal strains.
Giordano and Kleiven [32]	Anisotropic, visco-hyperelastic.	The mechanical anisotropy is directly related to FA map using a custom developed mathematical relation to describe fiber dispersion parameter. Mapped multiple DTI voxels per FE.	Overprediction of the extent of the injury by the first principal strain was dependent on the loading direction with respect to the orientation of the fibers.
Giordano et al [4,33]	Anisotropic, visco-hyperelastic.	An affine registration between the DTI brain and the obtained voxelized FE brain mask is implemented. Mapped multipled DTI voxels per FE using a weighted averaging method.	Anisotropic brain significantly lowered strains in axonal directions and increased maximum principal strains for anisotropic regions of the brain. Found the strain in axonal direction to be a better injury predictor than MPS, AESM, CSDM, BrIC and HIC.

Abbreviations: FE, finite element; WM, white matter.

information derived from the imaging data.[4,27–33] Some of the studies[4,26,27,30–33] mapped multiple voxels from diffusion tensor imaging data to a single element in the finite element model to account for the differences in the number of voxels and mesh elements. This resulted in the use of a weighted-averaged fiber orientation or fractional anisotropy measure per element. The axonal strains (i.e., the strains calculated in axonal fiber bundle direction) were determined using post-processing measures. For example, Chatelin et al[26] projected the strains from the bulk volume elements onto the fiber directions derived from diffusion tensor imaging after the finite element simulation. However, adopting an averaged description of fiber orientations and fractional anisotropy values per element may also cause a loss of axonal strain information and thereby compromise the accuracy of the material model. This occurs because an averaged direction may not be aligned with the true orientation of the axonal fiber bundles. This problem can be addressed by developing novel modeling methodologies that can replace these averaging procedures and reduce the loss of anatomical resolution. In this direction, most recent work by Zhao et al[35] used diffusion tractography models to obtain axonal directions and used them (without any averaging procedures) to calculate axonal strains—thus improving the resolution of the axonal fiber network that can be included in the head model. They used an isotropic model to represent the brain tissue, which might affect the axonal strain response.[28] This idea could be further improved by developing new methodologies to generate the anisotropic description of the brain tissue while maintaining the same level of anatomical resolution (that is possible by the exact use of fiber orientations obtained from tractography models instead of adopting averaging procedures).

One approach to include anisotropy using the diffusion tractography models could be implementing them as explicit fiber network models. Individual fibers can be implemented as a set of truss or beam elements explicitly into the brain tissue. This technique was investigated by Zhang et al[36] where they developed a 3D model of fiber network embedded in an elastic matrix. A continuous meshing approach was used (where the fibers and the matrix are meshed together such that there are shared nodes between fiber and matrix elements). However, the shared node meshing procedure will be expensive for large models and would be difficult to adopt because of the complex network of axonal fibers. Therefore, in this study, we investigate the applicability of the embedded element method

as an alternative numerical approach to model the complex network of fibers present in the brain.

The embedded element method, also called the "s-element method" or the "superimposed mesh method," was first developed by Ortiz et al[37] and Belytschko and Fish.[38,39] Over the past decade, a number of modeling applications using the embedded elements were published.[40–47] Some used this technique to develop nonlinear finite element analysis of reinforced concrete structures[40,41] while some other studies[42,44,46,47] applied this technique to develop finite element models of textile composites. Korunovic et al[43] used this method to embed surface elements with rebar layers into the volume elements of tire mesh to implement its composite characteristics. Lin et al[45] used this method in developing representative volume elements of 3D collagen scaffolds. These representative volume elements were used to tune the mechanical properties of these scaffolds. To the authors' knowledge, there have been no reports on the utilization of the embedded element method in modeling the brain tissue.

The novelty of this work lies in applying this embedded element technique to model the brain. Diffusion tractography models were included in the brain model explicitly for the first time to incorporate anisotropic behavior into the brain tissue. This embedded element technique enables the direct incorporation of axonal tractography model into the human head model without any complicated pre-processing steps. The primary advantage of this method is that it accommodates information from multiple voxels of diffusion tensor imaging into a single volume element without any averaging procedures. Other advantages include increased spatial resolution of the white matter finite element model, anisotropic stiffening of brain tissue without the use of advanced constitutive laws, direct computation of axonal strains without the need for post-processing steps, and improved insight into the behavior of anatomically important individual axonal fiber tracts. Additionally, this method does not introduce an overly burdensome computational cost.

The specific objectives of this study are as follows: (1) to apply and explore the embedded element method as a viable numerical approach for white matter modeling in the brain; (2) to implement this approach and examine the axonal strain damage predicted by model compared to other existing injury criterion; and (3) to apply this approach and conduct a quantitative analysis examining the influence of impact direction and overall axonal orientation on the extent of injury.

The layout of this paper is as follows. Section 2 introduces the theoretical framework of the embedded finite element method. Section 3 demonstrates validation of the head model and presents results of the finite element analysis of the human head with embedded axonal tractography under various impact loading conditions. Section 4 provides a discussion of the results, and Section 5 closes with concluding remarks and recommendations for the future course of work.

2 | METHODS

A suite of medical imaging and software tools was used to obtain an individual-specific finite element model of the human head. Figure 1 shows a schematic of the complete process. Magnetic resonance imaging (Figure 1A) and diffusion tensor imaging (Figure 1B) scans of a female soccer player were obtained from the Pennsylvania State University Center for Sports Concussion Research and Service (www.concussion.psu.edu). The imaging data were parceled and segmented as shown in Figure 1C. The diffusion tensor
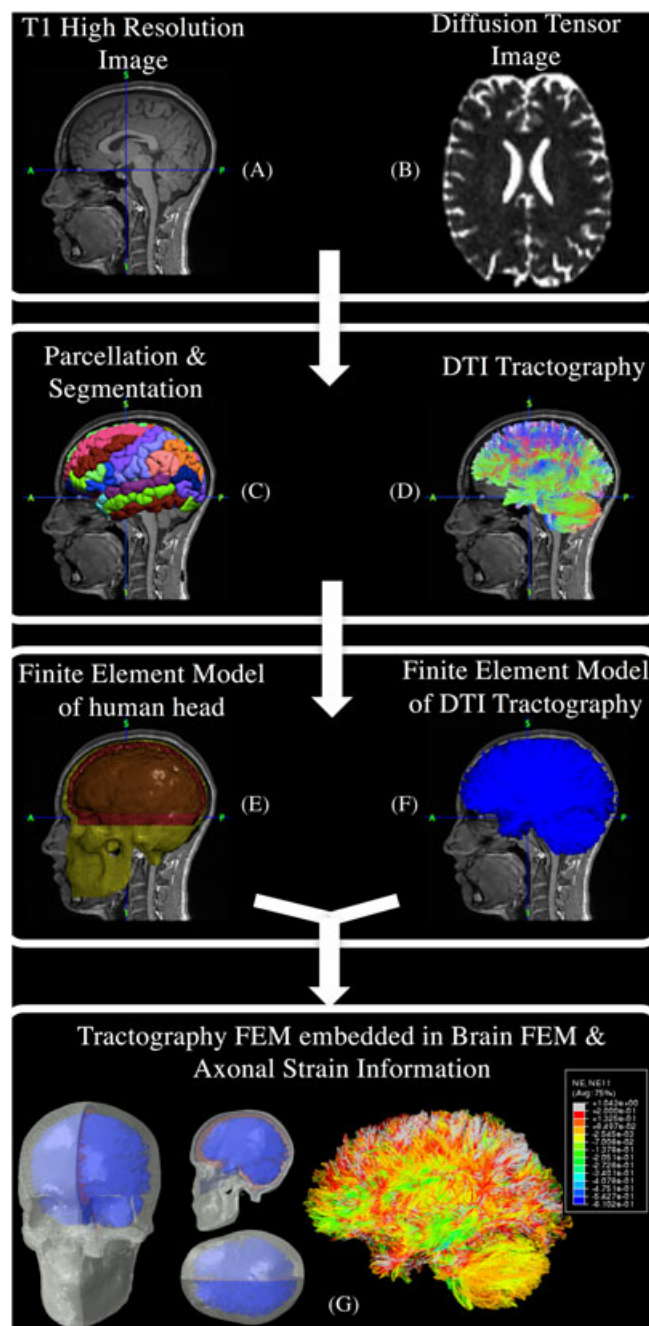
FIGURE 1 Process flowchart adopted in this paper. A, MRI scan. B, DTI scan. C, 3D surfaces. D, DTI tractography. E, Human head finite element model. F, DTI tractography finite element model. G, Tractography embedded into the human head finite element model

tractography model was obtained by processing diffusion weighted imaging scans, as shown in Figure 1D. This anatomical information was then used to generate a finite element model as seen in Figure 1E,F. The axonal fiber finite element model was incorporated into the human head model. Figure 1G displays the incorporated tractography and the respective finite element analysis under impact loading conditions. We discuss each of the above steps in more detail shortly.

The imaging data, shown in Figure 1A,B, were acquired with a 3-Tesla magnetic resonance imaging scanner (Magnetom TrioTim; Siemens, Erlangen, Germany). In total, 45 axial slices covering the whole brain were obtained with a voxel size of 3.0×3.0 mm and a slice thickness of 3.00 mm. A repetition time of 5900 ms and an echo time of 99 ms were used as timing parameters. The data were acquired using 30 different diffusion directions (collected with a sequence of b values b = 0, 1000, 2000 s/mm^2).

These data were used to the create 3D anatomical components of the human head by labeling and segmenting the voxels into different anatomical components, such as the scalp, skull, cerebrospinal fluid, and brain (Figure 1C). The axonal fiber tractography was then developed from the diffusion tensor imaging using the fiber tracking procedure, as shown in Figure 1D. Whole brain fiber tracking was performed using the Diffusion Toolkit (www.trackvis.org/dtk) and TrackVis (www.trackvis.org,[48]) software tools, which use a standard fiber assignment by continuous tracking approach to reconstruct fiber paths.[49] Before starting the tracking process, Digital Imaging and Communications in Medicine (DICOM) images were converted into the NIfTI format,[50] and the diffusion gradient directions were extracted with the *dcm2nii* script.[51] The Diffusion Toolkit was then employed to construct track files from the image set using an axial image orientation option and an angle threshold of 35 degrees.[52–55] Tracking was terminated when 2 consecutive moving fibers had an angle above this threshold. Track files generated by Diffusion Toolkit were then loaded into Trackvis for visualization. Fibers shorter than 18 mm were discarded,[53] and an image mask on the basis of the b0 image (NIfTI format) was used. The resulting tractography had 17 001 fiber tracts present in the model with a maximum length of 171.776 mm, a minimum length of 18.006 mm and a mean length of 43.7349 ± 23.239 mm. Figure 2 shows the distribution of fiber tracts on the basis of their lengths.

Following the generation of surface files for different anatomical components, high-quality finite element meshes were generated as shown in Figure 1E. Multiblock meshing techniques were used to develop hexahedral meshes for the brain, cerebrospinal fluid, and skull. This meshing procedure was performed using ANSYS ICEM CFD 14.5.7 (Ansys Inc, Canonsburg, PA, USA).

A structured mesh block system of the brain was developed according to the brain's surface geometry. Once the block structure was formed, as shown in Figure 3, mesh smoothening procedures were adopted to improve the overall mesh quality of the brain. The final hexahedral mesh developed for the brain is shown in Figure 4. Various types of mesh quality metrics are shown in Figure 5. In summary, the total number of hexahedral elements in the brain mesh were 153 328. More than 99% of elements had a determinant greater than 0.5, with 88% of elements showing a determinant greater than 0.8. Only 1.925% of elements had orthogonal quality less than 0.6. Most of the elements had a skew quality greater than 0.6. Only 0.02% of the elements had a minimum angle less than 30 degrees (worst minimum angle is 25.4 degrees), and 99.98% of elements had a maximum angle less than 150 degrees (worst maximum angle is 153.6 degrees). Furthermore, 0.074% of the elements had a warpage over 45 degrees (maximum warpage is 81 degrees). Definitions of the above quality metrics were provided in Appendix A.

The axonal tractography obtained from TrackVis software was converted into a finite element model comprising truss elements using a custom MATLAB script (Figure 11F). Each fiber in the finite element model was represented by a mesh of truss elements. The number of truss or beam elements per fiber varied depending on the total length of the fiber. The axonal fiber tractography was modeled using a total of 161 811 truss elements. Figure 6 shows the fiber tractography, the corresponding finite element model developed using the MATLAB script, and a single fiber mesh of 21 truss elements. Each of these truss elements represent a section of the axonal bundle along its axis and are assumed to have a circular cross section with their diameter representing the typical diameter of axonal fiber bundles. The diameter was chosen to be 1.12 ± 0.08 mm, on the basis of the study by Guy et al[56] in which axonal dimensions of the guinea pig optic nerve were reported. This diameter was used to describe all the axonal fiber bundles in this model.
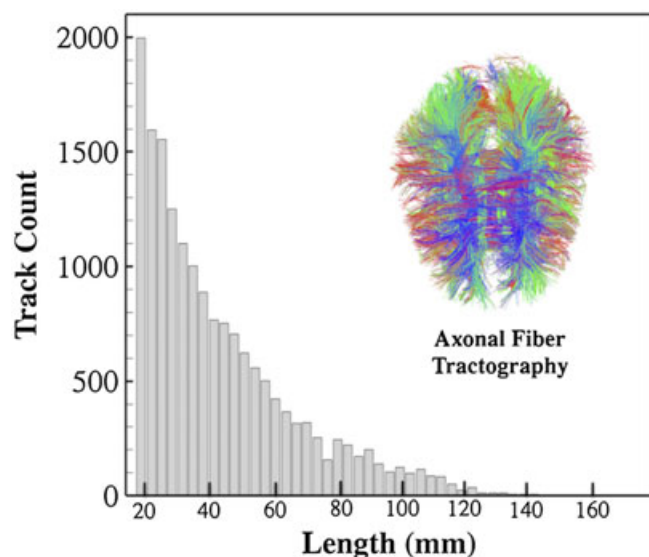
FIGURE 2 Length-wise distribution of fiber tracts in the tractography model
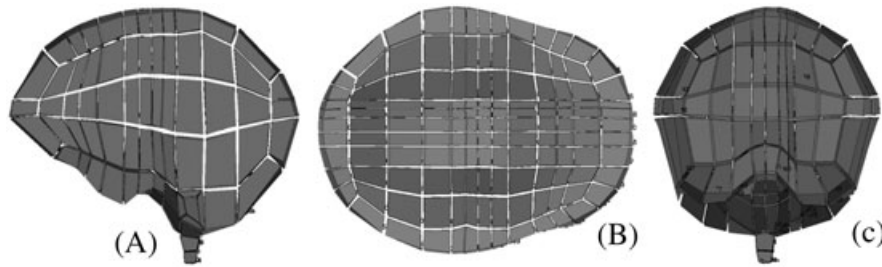
FIGURE 3 Blocking structure (used for brain mesh) in different views. A, Blocking structure—sagittal view. B, Blocking structure—axial view. C, Blocking structure—coronal view
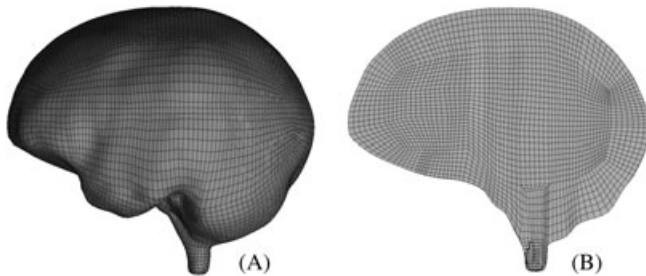
FIGURE 4 Hexahedral mesh developed for brain. A, Brain surface mesh. B, Brain volume mesh

The axonal fiber network was then incorporated into the brain mesh using the embedded element method. In embedded element method, a composite material model is adopted where the reinforcements and matrix are meshed separately, and then assembled with appropriate constraints. These constraints are used to specify that an element or group of elements is embedded within a host element or a group of elements. If the node of an embedded element lies within a host element, the node becomes an "embedded node," and its translational degrees of freedom are constrained to the interpolated values of the corresponding degrees of freedom of the host element. Using linear interpolation, the displacements at any point within a host element are[57]

$$u^m = \sum_{i=1}^{q} N_i^h u_i \tag{1a}$$

$$v^m = \sum_{i=1}^{q} N_i^h v_i \tag{1b}$$

$$w^m = \sum_{i=1}^{q} N_i^h w_i \tag{1c}$$

where u_m, v_m, and w_m are the X, Y, Z displacements of the embedded node, and u_i, v_i, and w_i, $i = 1, 2,...q$ are the corresponding nodal displacements of the host elements. The N_i^h are the shape functions for the host elements (superscript h indicates that the shape functions belong to the host element). Assuming a no-slip condition between the embedded element and the matrix, the nodal displacement of the embedded element will be same as the displacement at any point in the matrix[58]:

$$\mathbf{u}_{\text{embedded}} = \begin{pmatrix} N^h & 0 & 0 \\ 0 & N^h & 0 \\ 0 & 0 & N^h \end{pmatrix} \mathbf{u}_{\text{host}} \tag{2}$$

Here, $\mathbf{u}_{embedded}$ is the displacement vector of embedded element, and $\mathbf{u}_{host}$ is the displacement vector of the host matrix. This formulation is available in ABAQUS Explicit 6.13-2 (Dassault Systémes Simulia Corp., Providence, Rhode Island, USA) with the *EMBEDDED option.

Two different meshes exist while using this method. Because both brain tissue and axonal fibers were extracted from the same image set, both meshes were pre-aligned. An embedded element constraint was then implemented in the model with 3D hexahedral elements of the brain tissue as the host elements and 1D truss elements of the axonal fibers as the embedded elements. Figure 7 shows the tractography model embedded inside the human head geometry. Two different dependency studies were conducted—one for the hexahedral mesh (brain tissue) and one for the truss mesh (axonal fiber bundles)—to determine the best possible mesh densities that could be used while still delivering accurate results. In the first case (the dependency study on the hex mesh), the average axonal strains obtained with hex meshes of different densities were examined, and a satisfactory mesh density was selected. The occipital loading conditions from Hardy et al[59,60] were used as input during this dependency study. In the second case (the dependency study on the truss mesh), a similar procedure was followed. Here, the mesh density selected in the first case was used to describe brain tissue in simulations. Different mesh densities of the tractography mesh were used in simulations, and the corresponding average axonal strains were studied to determine the best possible mesh density.

Material properties employed in the model are listed in Table 2. An isotropic elastic material model was used to describe the skull and skin tissues. The pressure response of the cerebrospinal fluid was modeled using a Mie-Gruneisen equation of state, with the deviatoric behavior modeled by defining a shear viscosity. The material properties of cerebrospinal fluid were chosen to be similar to that of
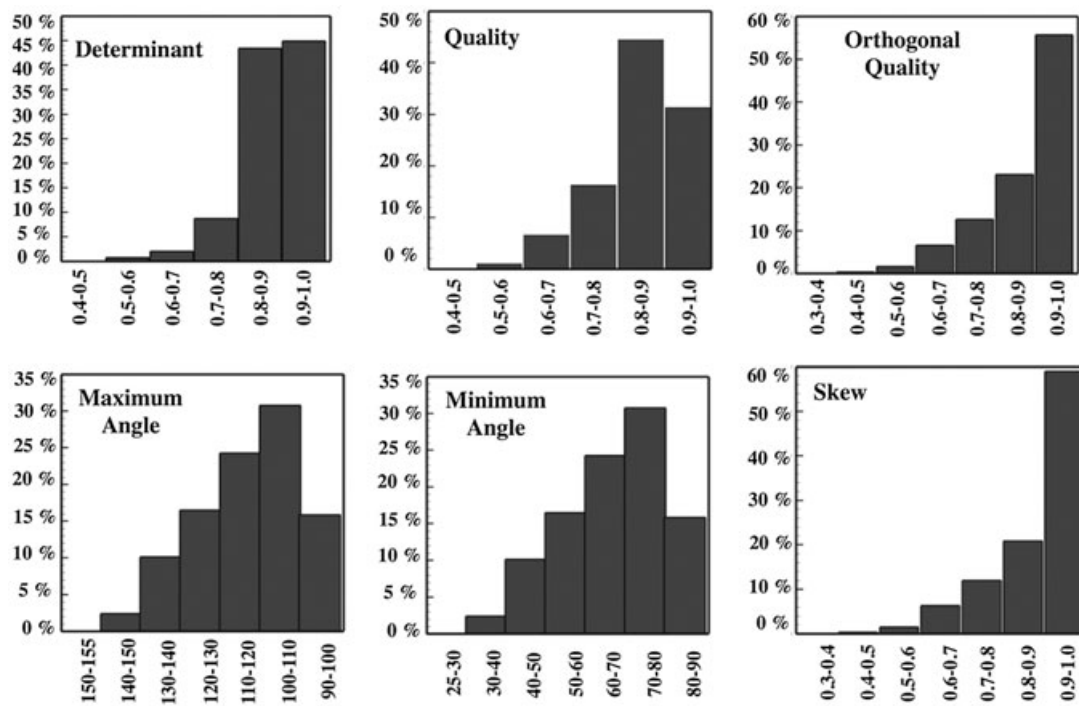
FIGURE 5 Quality obtained for the hexahedral brain mesh. Different quality metrics like determinant, quality, orthogonal quality, maximum angle, minimum angle, and skew were plotted for the brain mesh. Definitions of these quality metrics are listed in Appendix A
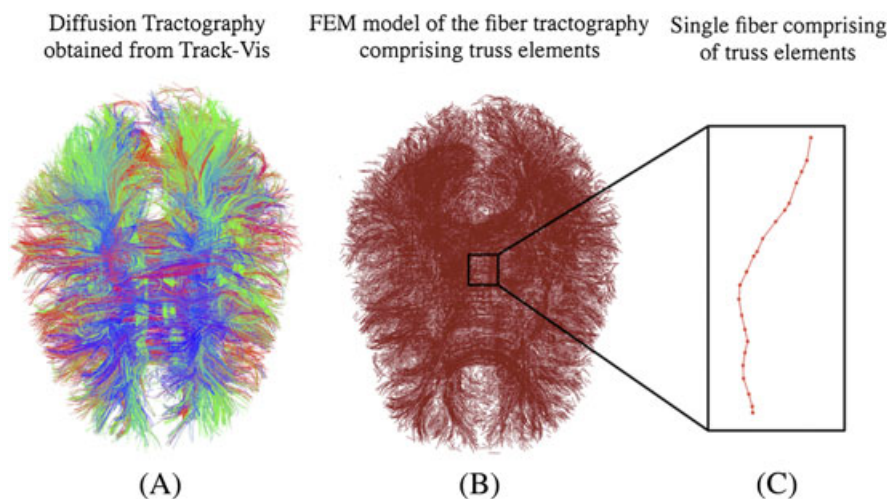
FIGURE 6 A, Diffusion tensor imaging tractography. As is customary for the display of white matter fiber tract orientation, fibers oriented anterior to posterior were colored green, superior to inferior as blue, and left to right as red. Fibers that have directions and were linear combinations of those directionalities were colored with a corresponding combination of colors according to the degree to which they are oriented in each of the standard directions. B, Finite element mesh of the tractography with each fiber comprising a set of truss elements. C, Single fiber comprising 21 truss elements

water.[29,61–63] A Mooney-Rivlin hyper-viscoelastic material model was used to represent the brain tissue matrix, and an Ogden hyperelastic material model was used to represent the axonal fibers. The material properties for both the axonal fibers and the brain tissue matrix were obtained from the stress-stretch summary curves provided by Chatelin et al[64] The viscoelastic parameters for the brain tissue matrix were identified from the experimental relaxation data in a shearing dynamic mechanical analysis by Shuck et al,[65] which did not take fibers into account.

Subsequently, confidence in the finite element model and material properties was established by comparison of the results from this model to the commonly used experimental studies of Nahum et al[66] and Hardy et al[59,60] for pressure and displacement verifications, respectively. For pressure verification, 1 of the 6 cases from a study by Nahum et al[66]—a frontal impact case, i.e., case 37—was used to verify the predicted brain pressure in the model. Here, the Frankfort anatomical plane of the human head was inclined at an angle of 45 degrees to the horizontal plane before impact. The
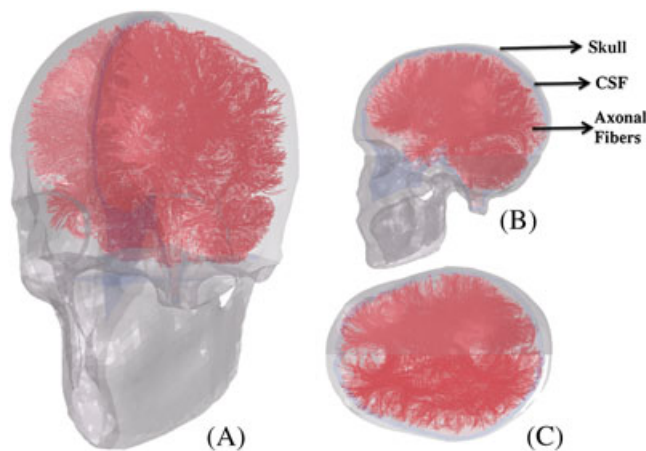
FIGURE 7 Tractography incorporated into finite element head model. Because both the 3D surfaces as well as the diffusion tractography information were extracted from the same image set, explicit mapping schemes were not required to spatially locate both the meshes (hexahedral human head mesh and 1D tractography finite element mesh). CSF, Cerebrospinal fluid

impact was made in a posteroanterior direction in line with the center of mass, which resulted in purely translational motion.

The detailed force and head acceleration time histories were reported for this case. The impact force and the pressure distribution in correspondence with the frontal area of the skull were considered as reference parameters for the validation. The impact force over time was used as input on the skull elements of the frontal bone in an anterior-posterior direction in the mid-sagittal plane. The intracranial pressures in the brain tissue region were calculated by averaging the pressures over certain number of elements. Averaging the pressures might give us a more generalized pressure response of the region.

For displacement verification, brain-skull relative displacement data from Hardy et al[59,60] was used to verify the predicted displacements from the simulation. The displacements were extracted at specific nodes in the model selected on the basis of the location of neutral density target's (NDT) reported by Hardy et al.[59,60] Figure B.1 shows the input accelerations for the 3 cases used in this procedure—i.e., frontal impact (C383T1), occipital impact (C755T2), and parietal impact (C393T4) conditions. These accelerations were applied to the center of mass of the human head with the skull treated as a rigid body.

Once validated, this model was then verified for evidence of injury in an actual concussive impact case. For this purpose, a concussive impact curve of a high school-level football athlete from a study by Ji et al[34] (case 9218) as shown in Figure 1G was used in the impact analysis on this model. Figure B.2 shows the input accelerations applied to the center of mass of the head model corresponding to this loading curve. For the subsequent injury analysis, an axonal injury threshold must be chosen. Several head injury thresholds were reported in the literature over time, e.g., both tissue level stress and strain threshold values.[14,19,67–71] An experimental study by Bain et al[69] reported the strain threshold for the onset of electrophysiological impairment of axons to be around 18%. This value is used as our injury criterion similar to that of Wright and Ramesh.[28] To implement the strain injury into our model,

TABLE 2 Table showing different anatomic components, material models and corresponding material parameters used in the finite element model

| Anatomical Components	Material Model	Material Parameters	References
Skin/scalp	Elastic	$\rho = 1130$ kg/m^3	[30]
		$E = 100$ kPa	
		$\nu = 0.45$	
Skull	Isotropic elastic	$\rho = 2100$ kg/m^3	[30]
		$E = 15$ GPa	
		$\nu = 0.229$	
Cerebrospinal fluid	Mie-Gruneisen equation of state	$\rho = 1000$ kg/m^3	[19]
		$C_0 = 1489$ m/s	
		$s = 1.79$	
		$\Gamma_0 = 1.65$	
		$\eta = 0.001$	
Brain tissue (matrix)	Mooney-Rivlin hyperelastic	$\rho = 1040$ kg/m^3	[64]
		$C_{01} = -1.034$ kPa	
	Viscoelastic	$C_{10} = 7.803$ kPa	[64]
		$K = 2.1$ GPa	
		$g_1 = 0.65425$	
		$\tau_1 = 0.0066940$	
		$g_2 = 0.0149$	
		$\tau_2 = 0.15642$	
Axonal fibers	Ogden hyperelastic	$\rho = 1040$ kg/m^3	[64]
		$\mu = 35.64$ kPa	
		$\alpha = 6.101$	
		$D = 9.1\text{e-}10$ Pa^{-1}	
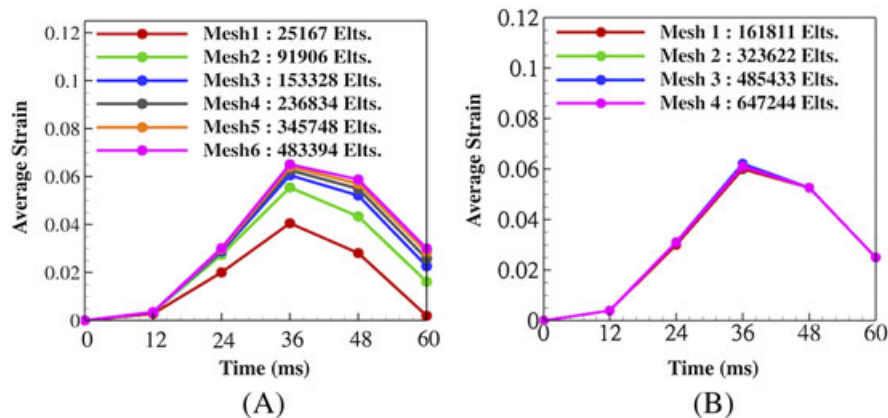
FIGURE 8 Mesh dependency plots for both hexahedral and truss meshes. A, Mesh convergence plot for hexahedral mesh. The difference between the results for the finest mesh (i.e., Mesh 6) and the next finer mesh (i.e., Mesh 5) is less than 5% (achieving convergence). Mesh 3 is used in further analysis in this work because the difference in results between this mesh and Mesh 6 is less than 8%. B, Mesh convergence plot for truss mesh. The difference in average strain readings between the finest mesh (i.e., Mesh 4), and the coarse mesh (i.e., Mesh 1) is less than 8%. Mesh 1 is used in further analysis

logarithmic strains in each of the truss elements were measured and compared to the injury threshold mentioned above. The logarithmic strains measured in each of the truss elements can be considered as a measure of axonal fiber strain.

Following the injury analysis, a preliminary analysis was performed to establish the importance of directionality in the injury analysis. Previous literature has shown that the seriousness of the injury varies with the impact direction (or head rotation). Therefore, to understand the influence of head rotation on the axonal injury, 3 simulations were perforemed. These include rotational acceleration applied to the center of mass of the model in 3 distinct planes, i.e., axial, coronal, and sagittal. A peak rotational acceleration of 5000 rad/s^2 was applied in the 3 simulations respectively. Extent of the axonal injury (percentage of damage) was studied and compared to understand the differences among the 3 simulations. At the same time, an attempt was made to understand the role of axonal arrangement (orientation) in the differences observed among the 3 simulations. A "heat map" of orientations of all the truss elements in the fiber network was developed (using custom MATLAB script) for this purpose. This map was developed on the basis of the orientations calculated in the spherical coordinate system using cartesian coordinate information (using the standard cartesian to spherical coordinate system conversion formulae).
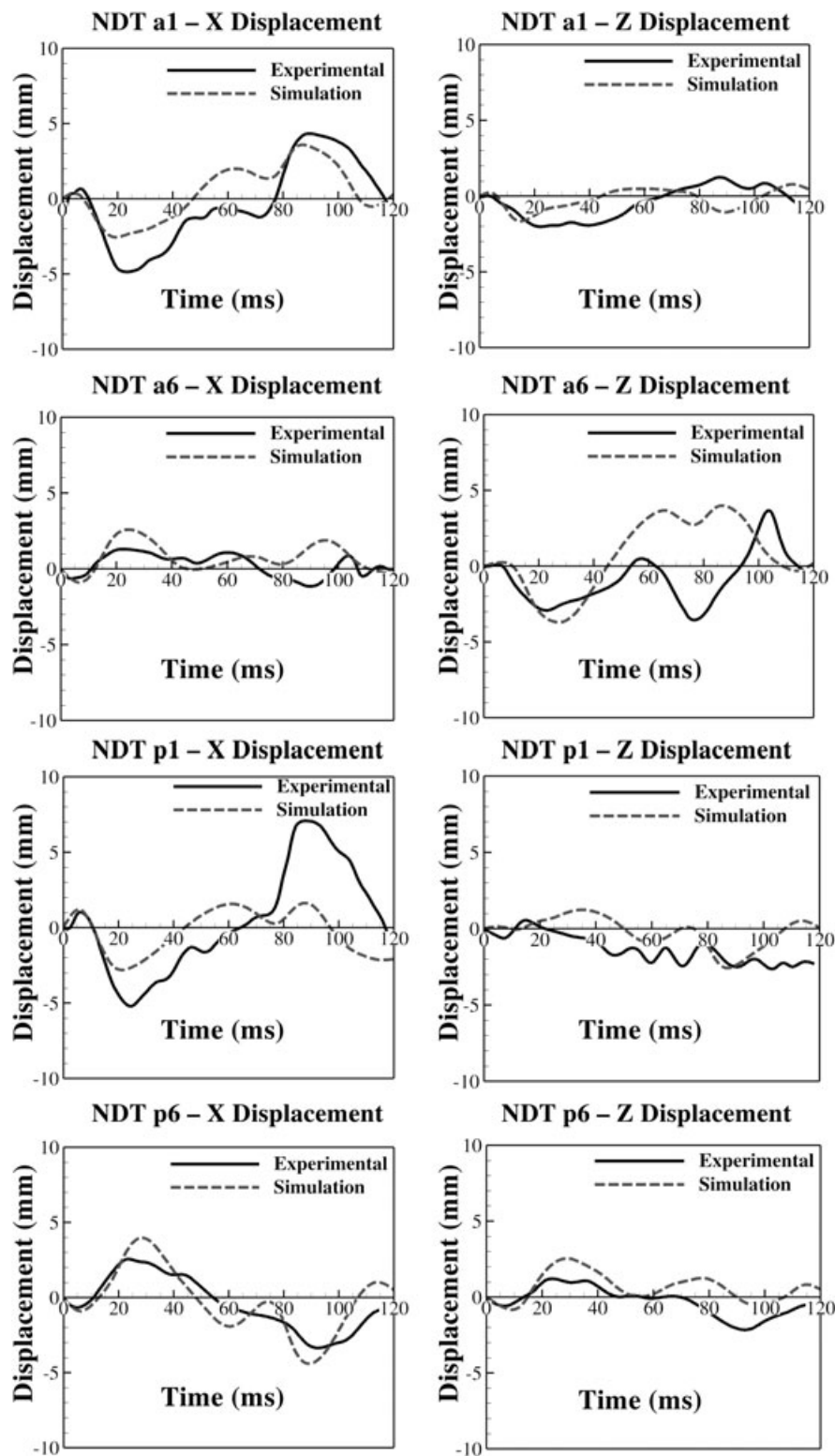
3 | RESULTS

Figure 8 shows the mesh dependency plots for both the hexahedral mesh (used to describe brain tissue) and the truss mesh (used to describe axonal fiber bundles). Both these plots show the average axonal strain at different time instants for various mesh densities. Figure 8A shows the dependency plot for the hexahedral mesh. The variation in the results obtained with the finest mesh (i.e., Mesh 6) and the mesh immediately next to the finest one (i.e., Mesh 5) is less than 5%. Hence, we
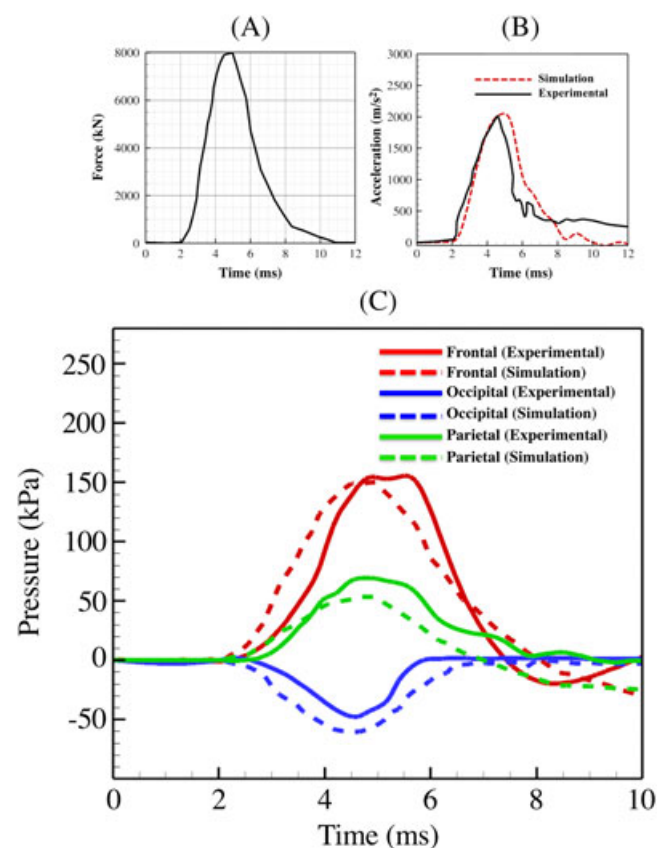
FIGURE 9 Nahum's pressure validation process. A, Plot showing the impact loading curve for the simulation. B, Plot showing an agreement between the simulated human head acceleration over time and experimental result. C, Plot showing an agreement between various intracranial pressures (simulated) and experimental results

can reasonably assume that the study reached convergence. The difference in results obtained from the dense mesh (i.e., Mesh 6) and coarse mesh (i.e., mesh 3) is less than 8%. In the subsequent analysis, the Mesh 3 (with a total of 153 328 elements) was adopted. Figure 8B shows the dependency plot
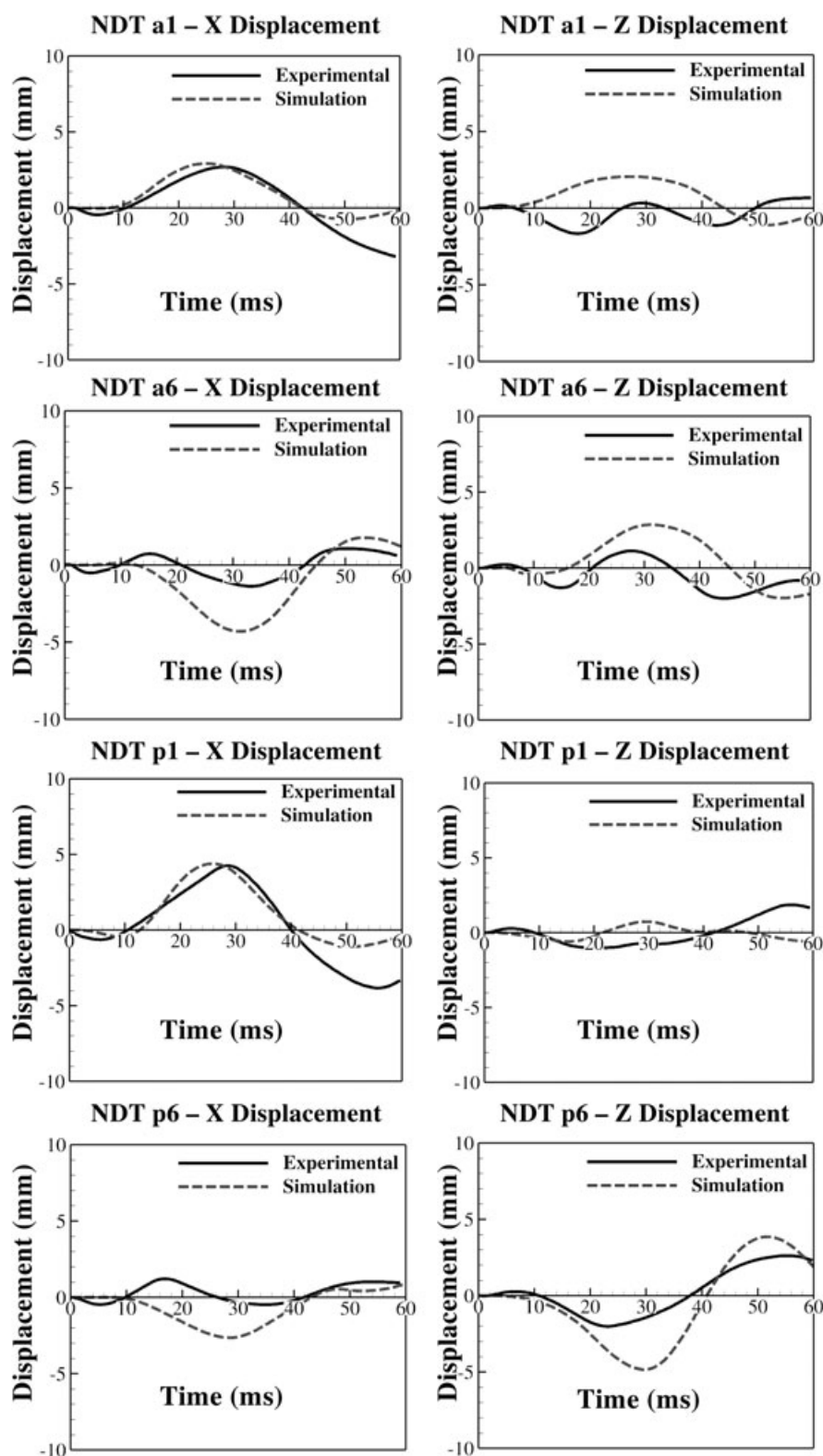
FIGURE 10 Comparison of experimental and simulated relative displacements between skull and brain for frontal loading condition. Case: C383 T1

for the truss mesh. The difference in results between the finest mesh (i.e., Mesh 4) and the coarsest mesh (i.e., Mesh 1) is less than 5%. For further analysis, Mesh 1 (with a total of 161 811 elements) was adopted.

Following the mesh convergence studies, the model was verified using results from the experimental pressure and displacement studies by Nahum et al[66] and Hardy et al,[59,60]

respectively. Figure 9 shows a comparison of the intracranial pressure curves obtained during simulations over time with the experimentally recorded values. Figures 10-12 show a comparison of the brain-skull relative displacement curves over time with the experimentally observed results for frontal (C383T1), occipital (C755T2), and parietal (C393T4) impacts published by Hardy et al.[59,60]

FIGURE 11 Comparison of experimental and simulated relative displacements between skull and brain for occipital loading condition. Case: C755 T2

After the validation, the model was subjected to the loading condition taken from a study by Ji et al.[34] The deformed configurations of the human head, as well as the axonal structure, are shown in Figure 13 in axial, coronal/lateral, and sagittal views at different time instants. It shows the logarithmic strains experienced by the axonal tractography embedded into the human head. The logarithmic strains are those measured in each truss element of an axonal fiber. This head impact simulation took about 5 hrs. on 16 processors to reach 40 ms. In this figure, the regions dominated by red are under tensile strains, and the regions dominated by blue color are under compressive strains. Figure 14 shows the corpus callosum
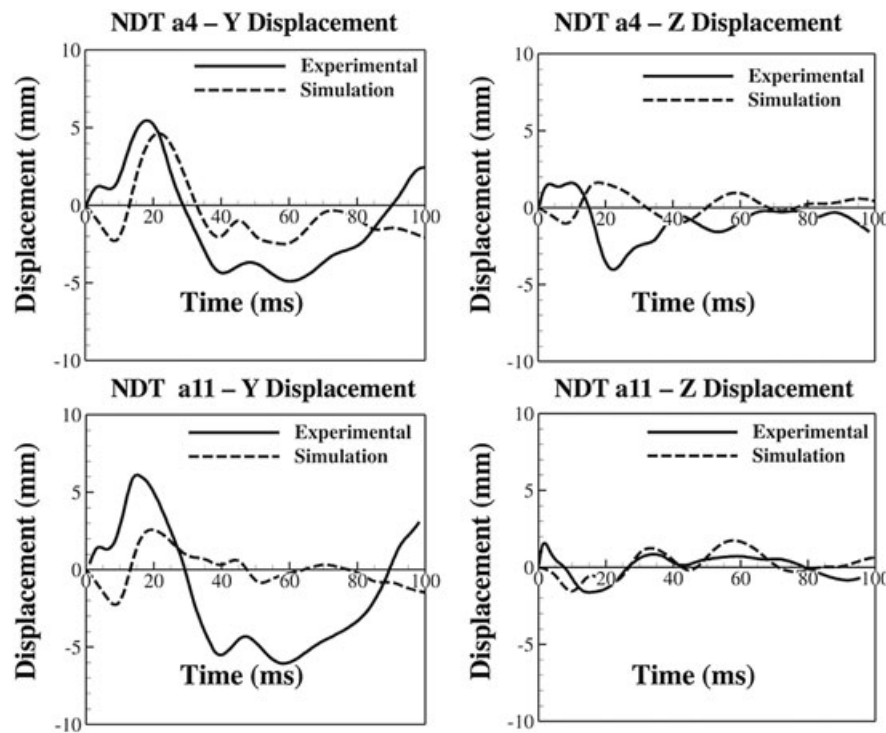
FIGURE 12 Comparison of experimental and simulated relative displacements between skull and brain for parietal loading condition. Case: C393 T4

region of the fiber network. A maximum strain of 20% was observed in this region. This figure demonstrates the higher resolution of the model that can be achieved using this approach.

Several injury criteria were reported in the literature. Out of those, commonly used injury criteria include maximum principal strain, shear strain, and von Mises stress. Figure 15 shows a comparison of the percentage of the cumulative damage of white matter observed using various injury criteria and also shows a table listing thresholds for those criteria. Percentage of cumulative volume damage at a time instant is defined as the percentage of damaged volume over the course of simulation until that particular time instant. An element is considered damaged if it experiences a strain/stress greater than the reported thresholds during that time. For the maximum principal strain measure, the brain tissue was considered to be damaged if the maximum principal strain in that region had exceeded a strain threshold of 31%, which was the injury tolerance threshold for mild diffuse axonal injury observed by Deck et al.[72] Axonal strain injury criterion of 18% was used as a threshold for predicting damage in the axonal fibers. For the shear strain measure, a shear strain threshold of 25% was used as proposed by Deck et al.[72] For von Mises stress, a threshold of 14.8 kPa was used as proposed by Yao et al.[67] During these cumulative damage calculations, a region damaged once is considered as permanently damaged and cannot become undamaged. Also, all the thresholds except the axonal strain injury criterion were used in the injury analysis by comparing them to the respective strain measures in bulk elements.

Among the injury thresholds used, shear strain predicted the maximum cumulative volume damage (34.80%) followed

by maximum principal strain (6.26%), axonal fiber strain (1.44%), and finally the von Mises stress (0.58%). The damaged regions of the brain calculated using different injury criteria are shown in Figure 16. This figure shows a substantial difference in the location/extent of the predicted damage using different injury criteria.

Following the injury analysis, a preliminary study showing the importance of axonal orientation in the extent of axonal injury caused because of different head rotations was performed. Figure 17 shows a "heat map" of the percentage of truss elements (which make up the axonal fiber bundles) with a given orientation developed using a local spherical coordinate system. This map will be used in the following study to explain the influence of orientation of different truss elements (and hence axonal fiber bundles) in the extent of damage observed during different head rotations. Figure 18 shows a comparison of the percentage of damaged fiber tracts, the percentage of cumulative volume damage and the percentage of number of damaged truss elements from axial, coronal and sagittal rotations of the human head finite element model respectively. In these simulations, a fiber tract is considered damaged if one of the truss elements experienced a strain greater than 18% during the simulation time. Axial rotation resulted in the largest percentage of damaged fiber tracts (10.39%) followed by coronal rotation (5.42%) and sagittal rotation (3.70%). A similar trend was observed when the percentage of volume of damaged truss elements was examined with axial rotation predicting the maximum damage (1.74%) followed by coronal (0.72%) and sagittal rotation (0.42%).
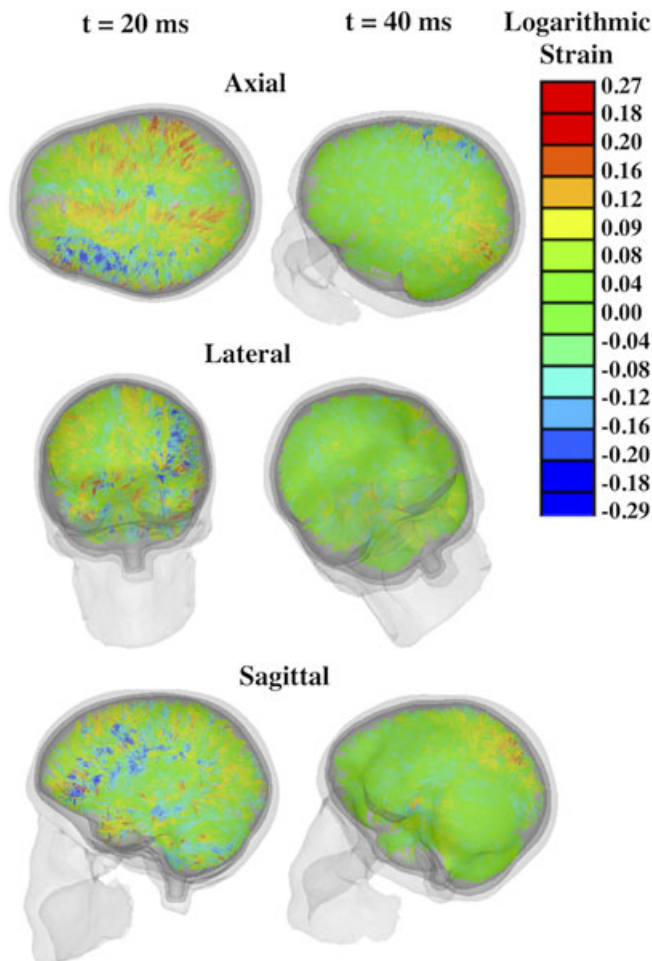
FIGURE 13 Deformed configurations of the human head at 2 different time instants, that is at $t = 20$ ms and $t = 40$ ms, in axial, lateral, and sagittal planes. The red color indicates a tensile logarithmic strain more than 18% in the respective truss elements whereas blue indicates a compression response in truss elements
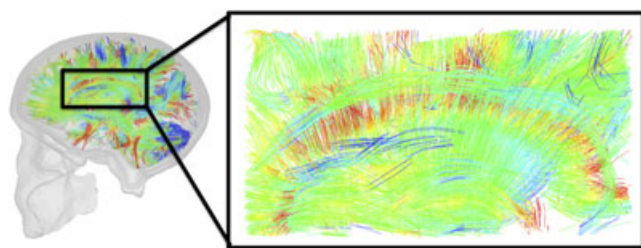
FIGURE 14 A zoomed in version of axonal fiber tracts and their corresponding mechanical response. This figure demonstrates the higher resolution of the head model possible in this approach

4 | DISCUSSION

In this study, the embedded element method was used to develop a human head finite element model with embedded axonal fiber tractography. Integrating an axonal bundle into a finite element model of a human head has been a focused area of computational modeling. Different averaging procedures, as well as the incorporation of orientation density functions, were previously used to account for the anisotropic
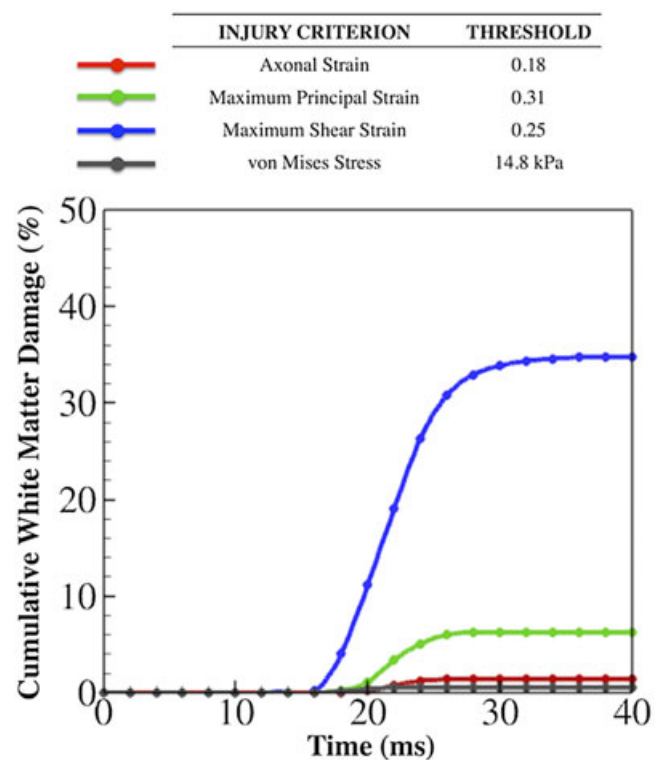

FIGURE 15 Comparison of percentage of cumulative volume damage of white matter over time using different injury criteria. Shear strain injury criterion predicted the maximum amount of cumulative volume damage followed by maximum principal strain, axonal fiber strain, and von Mises stress. Percentage of cumulative volume damage at a time instant can be defined as the percentage of total volume of the damaged elements till that time instant. An element is considered damaged if it experiences a strain/stress greater than the threshold specified during the simulation

orientation of the axons. With the method described here, we made progress in resolving the problem of incorporating the exact orientation of axonal fibers into the model and extracting axonal fiber strains without any post-processing measures. The primary focus has been to introduce a method that can be implemented using more readily available tools of commercial finite element packages.

This process has numerous advantages. The foremost benefit lies in using 2 independently meshed entities that superimpose each other instead of using a continuous mesh structure. This method enables us to incorporate multiple fiber orientations per element, resulting in the complete use of anatomical information as opposed to the limited data attained from considering a volume-averaged fiber orientation per finite element of the brain mesh. The incorporation of this axonal fiber structure automatically accounts for the directional stiffening behavior of the fibers in the brain tissue. Furthermore, this approach does not constrain the number of fibers or the fiber orientations that can be embedded in a given finite element model (relieving us of developing complex multifiber constitutive models[73]) yet remains relatively computationally inexpensive. An explicit modeling of the fiber tractography is possible. This enables us to track the complete trajectory of
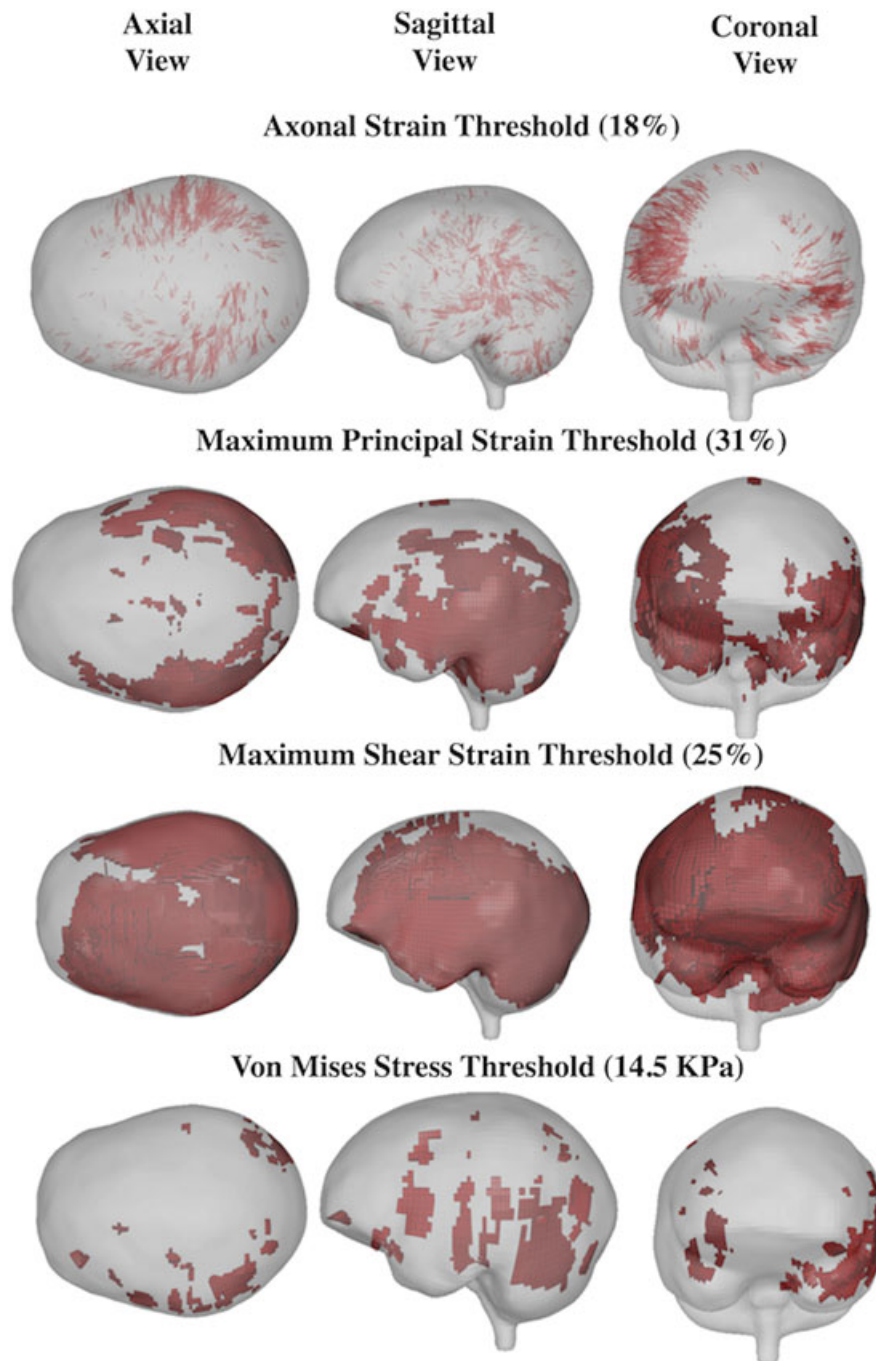
FIGURE 16 Comparison of damaged white matter regions (cumulative) using different injury criteria. Cumulative volume damage at a time instant can be defined as the total volume of the damaged elements till that time instant. An element is considered damaged if it experiences a strain/stress greater than the threshold specified during the simulation

the axonal fibers in the human head over time during impact or other external loading.

To ensure accuracy using this method, high-quality hexahedral meshes were generated, and the quality metrics were compared to previous studies.[23,74] Mesh dependency studies—for both hexahedral mesh and truss mesh—were performed to determine the coarsest mesh that can produce accurate results while maintaining computational efficiency. For the brain tissue (made up of hexahedral elements), Mesh 3 (average element side is 2.1 mm) was chosen on the basis of the dependency study; the simulation with this mesh takes

around 30% of the analysis time of the finest mesh, although the results are practically identical. For the axonal fiber network (made up of truss elements), Mesh 1 (average element length is 4.5 mm) was chosen on the basis of the dependency study; the simulation with this mesh takes almost 20% less time than that of the finest mesh, although the results are practically identical. After the mesh dependency studies, this model was successfully compared to experimental studies. Our results showed similar trends between the experimental observations and simulations. Note that the comparisons were performed with fibers embedded in the brain tissue matrix.
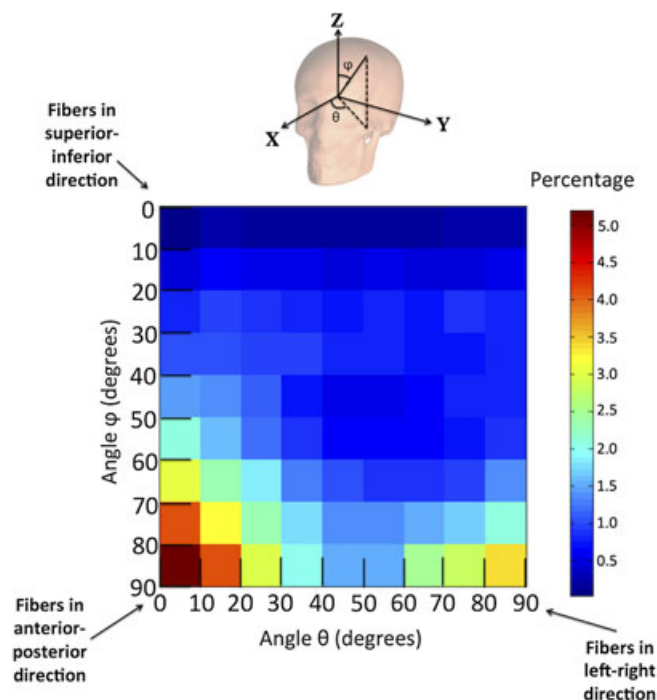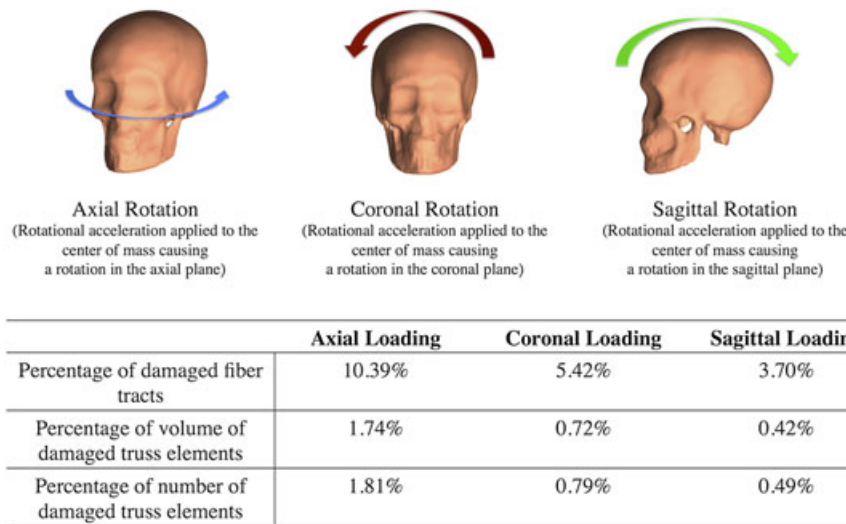
FIGURE 17 "Heat map" of percentage of truss elements with a given orientation developed using a local spherical coordinate system. The gray boxes in the map shows the percentages of fibers lying in different planes

A finite element analysis was performed using a loading curve from a sports-related concussion study by Ji et al[34] to explore the applicability of this embedded element technique in studying axonal injury. An exact representation of the fibers has been performed instead of using a volume-averaged fiber direction per finite element, thus eliminating the loss of axonal information. Shear strain criterion predicted the maximum cumulative damage (34.80%) followed by maximum principal strain (6.26%), axonal strain (1.44%), and von Mises stress (0.58%). This implies that a higher maximum principal or shear strain does not necessarily guarantee a higher axonal strain (axonal directions are different from the maximum principal or shear strain directions). A similar trend was observed by Wright et al[29] with shear strain criterion predicting the maximum damage followed by maximum principal strain. However, they observed an almost equal axonal damage using maximum principal strain and the axonal strain injury criteria. This difference in observations might be due to a lot of factors such as the exact use of axonal directions instead of averaged axonal directions, size and shape of the head, use of different loading conditions, and the use of 2D models in their analysis. The cumulative damage measurements using a threshold of 18% for both maximum principal strain (42%) and axonal strain (1.74%) are in close agreement with the 36% and 2% observed by Ji et al.[34]

Following the injury analysis, an heat map was prepared to examine the distribution of orientations of the different truss elements present in the fiber network. From this orientation map, we can see that the highest percentage of elements

are oriented in the anterior-posterior direction followed by elements oriented in the left-right direction. A very low percentage of elements are oriented in the superior-inferior direction. From this, we can hypothesize that axial rotation should cause more damage because it engages elements in both anterior-posterior direction and left-right direction (elements with $\phi = 90$ degrees). Similarly, we can also hypothesize that the damage that is caused by the sagittal rotation (engages elements in the anterior-posterior direction and elements in the superior-inferior) should be next, followed by damage from the coronal rotation (engages elements in the left-right direction and elements in the superior-inferior direction).

To examine the above hypothesis, an investigation was conducted to determine the influence of axonal bundle arrangement on the extent of injury under different head rotations. Axial rotation resulted in the maximum damage (concluded by observing different damage measures such as the percentage of damaged fiber tracts, the percentage of the volume of damaged truss elements, the percentage of number of truss elements). This agreed with our hypothesis. This also agreed with the recent work by Zhao et al[35] where they observed a maximum axonal damage during axial rotation. Coronal damage (percentage of damage from coronal rotation) is observed to be more than the sagittal damage (percentage of damage from sagittal rotation). Again, this result agrees with the recent work by Zhao et al[35] and experimental studies by Gennarelli et al,[75,76] which revealed that the incidence of traumatic unconsciousness with prolonged coma is longer in coronal plane rotations when compared with the same rotation in other 2 planes. But, this does not agree with the hypothesis drawn from the orientation map, i.e., sagittal damage should be greater than coronal damage. This behavior might be a result of the stiffening of the brain tissue in the anterior-posterior direction because of the presence of a large number of elements in this orientation. During sagittal rotation, this stiffening phenomenon might be more dominant, resulting in a smaller percentage of truss elements experiencing strains greater than 18% (which implies less damage). Figure 19 shows the heat map of damaged truss elements from axial, coronal, and sagittal rotations of human head respectively. From this Figure 19, it can be seen that axial rotation damaged elements oriented in anterior-posterior direction and elements oriented in the left-right direction. This agrees with our hypothesis. Similarly, the coronal damage is dominant in fibers oriented in the left-right direction, and the sagittal damage is more dominant in the elements oriented in the anterior-posterior direction, which again agrees with our hypothesis. This shows that the impact direction and the underlying brain fiber architecture are important factors in determining the vulnerability of different axonal fiber tracts to deformation beyond a threshold. It should also be observed the midline anatomical structures such as falx cerebri and tentorium cerebelli are absent in this model. Including these components could be significant in analyzing the effects of different head rotations and might provide us with a better

|	**Axial Loading**	**Coronal Loading**	**Sagittal Loading**
Percentage of damaged fiber tracts	10.39%	5.42%	3.70%
Percentage of volume of damaged truss elements	1.74%	0.72%	0.42%
Percentage of number of damaged truss elements	1.81%	0.79%	0.49%

FIGURE 18 Influence of head rotation. Comparison of percentage of damaged fiber tracts, volume percentage of damaged truss elements, and percentage of number of damaged truss elements among axial, coronal, and sagittal rotations

insight into the role of axonal fiber arrangement on the extent of the injury.

The above analyses and discussion showed the feasibility of the embedded element method in studying axonal injury. However, this method does have some limitations. The first limitation is the volume redundancy issue between the fiber and matrix meshes, causing an addition of additional mass and stiffness to the model. This issue can be resolved using the "s-version"[77] of the finite element method (consists of a patch of higher order elements in the mesh to resolve the structure of functions with higher gradients), the "independent mesh method"[47] (by disregarding the shape functions in the redundant regions) or the "domain superposition method (DST)"[46] (by subtracting the constitutive stiffness of the matrix from the constitutive stress-strain matrix of the embedded structures). The second limitation is the issue of the interpenetration of the axonal fibers among themselves during this approach, but it could be overcome by defining contact between the embedded elements. Recent work by Tabatabaei et al[44] used contact algorithms available in ABAQUS to avoid yarn (modeled as 3D meshes) interpenetrations while modeling textile composites using the embedded element method. At this point, ABAQUS Explicit does not support contact algorithms to be defined between 2 truss or beam elements (only works between a pair of 3D surfaces or between a 3D surface and truss or beam element). Therefore, no contact definition was used in the simulations presented in the paper. In future, the interpenetrations could be overcome by defining contact—when these algorithms are developed/implemented—between the embedded truss or beam elements. This problem could also be resolved by introducing a constant arbitrary gap between the embedded elements as shown by Jiang et al.[46] The third limitation is the use of truss elements to describe axonal fiber bundles. Truss elements can only account for the axial loading (tension or compression) and cannot accommodate

bending effects. This could adversely affect the axonal strains observed during the analysis. A beam element-based axonal tractography can be used to account for the bending strains in the axonal fibers, along with the compressive and tensile strains. However, at this point, beam elements with hyperelastic material properties cannot be used (elastic material properties can be used) in ABAQUS Explicit. Using elastic material properties might adversely affect the strain response of the axonal fibers. Due to this reason, beam elements were not used in this study to describe the axonal fibers. However, currently efforts are forthcoming to develop a detailed study on the differences between truss element-based (with hyperelastic material properties) and beam element-based (with elastic material properties) models. Some of the preliminary results were included in the Appendix C. The fourth limitation includes the use of no-slip and no-tortuosity assumptions (leading to an affine transformation of strain tensor from brain tissue to the axonal fibers). No-slip assumption may limit the accuracy of the strain measurements because the presence of slip might increase/influence shearing of the axons, thus improving the accuracy of the strain predictions. Efforts are enroute to include this in the future work. At the same time, because the analysis was performed at a "mesoscale" level (axonal bundle level and not single axon level), the authors believe that the tortuosity, observed mainly at microscale (single axon) level, might not affect the fiber strain predictions (which were obtained at "bundle" scale). Additionally, the authors also acknowledge the absence of the neck, ventricles, dura, falx, and tentorium that each play a crucial role in head biomechanics, particularly when axonal strain information is of interest. Efforts are forthcoming to include these details. However, all the simulations with longer duration (i.e., time >20 ms) were performed with experimentally observed accelerations applied to the center of mass of the model. The authors believe that this will compensate for the absence of the neck in the model. Additionally, the
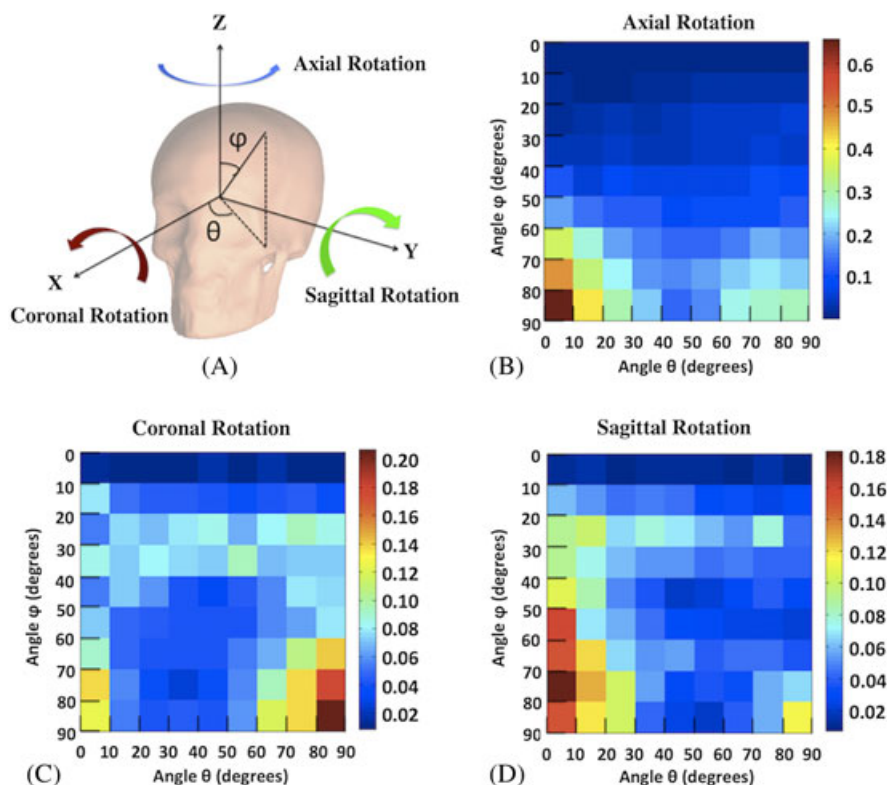
FIGURE 19 Orientation map of damaged truss elements from the following. A and B, Axial rotation. C, Coronal rotation. D, Sagittal Rotation of the human head model

diameter of all the axonal fibers is assumed to be around 1.12 mm, the same as guinea pig optic nerve, which simplifies the analysis.

Aside from the above improvements, some recommendations for the future include developing material models and element formulations that do not include the compressive resistance of the fibers. Validation of the finite element model with clinical results would improve the model's credibility. This can be done by correlating the white matter damage (changes in mean diffusivity, fractional anisotropy, fiber count, and fiber length) observed from the diffusion imaging[78] with that of the axonal damage predicted by the model. This would include gathering prescan and postscan of concussed individuals and having the means to quantitatively describe impact conditions. Such studies may be enabled by the use of impact sensors in sports.[79] In the future, these explicit tractography models can be used to study the influence of injury on the bioelectric behavior of the bundles. This might enable us to develop structure-function models of the human brain. Additionally, the explicit modeling of the fiber tracts can be useful in developing a time-evolving neurocomputational human head finite element model. Previously, Kraft et al[30] presented the idea of coupling the finite element model developed from diffusion tensor imaging with a connectome-based graph analysis to study the time-dependent evolution of structural network damage. This idea can be further improved by using time-dependent structural degradation results for individual fiber tracts (which is enabled by this method). In the

future it might also be useful to explore application of the embedded element method to model complex glial and vascular networks that have been reported to be important for understanding brain injury.[80]

5 | CONCLUSION

In conclusion, this research focused on developing a human head model with embedded tractography, which may be a useful technique to model axonal injury. Comprehensive strain analyses, to compare different injury criterion, were performed, and trends similar to that of previous research were observed. An investigation to determine the influence of impact direction on the damage has produced results similar to those of experimental studies. From this investigation, we concluded that the damage in the brain is dependent on the orientation of the fibers and the loading direction. In summary, a computational head model has been developed using readily available commercial tools, which provides a 3D analysis of fiber tract damage, resulting from direct impact to the human head. This tool can ultimately allow for an improved understanding of the axonal injury and may help us to develop better safety measures and diagnostic tools related to head injury.

COMPLIANCE WITH ETHICAL STANDARDS

The research being reported in this paper has been conducted in an ethical and responsible manner. The authors declare that they have complied with all the relevant ethical standards. The authors declare that the results being reported here are produced without any falsification, fabrication, or manipulation. They declare that this work is original and not plagiarized and has not been published elsewhere.

CONFLICT OF INTEREST

The authors declare that they have no affiliations with or involvement in any organization with any financial interest (such as honoraria; educational grants; participation in speakers' bureaus; membership, employment, consultancies, stock ownership, or other equity interest; and expert testimony or patent-licensing arrangements) or non-financial interest (such as personal or professional relationships, affiliations, knowledge, or beliefs) in the subject matter or materials discussed in the paper.

REFERENCES

1. Faul M, Xu L, Wald MM, Coronado VG. Traumatic brain injury in the United States. *Centers for Disease Control and Prevention, National Center for Injury Prevention and Control*, Atlanta, GA; 2010.

2. Smith DH, Meaney DF. Axonal damage in traumatic brain injury. *The Neuroscientist*. 2000;6(6):483–495.

3. Gennarelli TA, Spielman GM, Langfitt TW, Gildenberg PL, Harrington T, Jane JA, Marshall LF, Miller JD, Pitts LH. Influence of the type of intracranial lesion on outcome from severe head injury: a multicenter study using a new classification system. *J of Neurosurgery*. 1982;56(1): 26–32.

4. Giordano C, Cloots R, Van Dommelen J, Kleiven S. The influence of anisotropy on brain injury prediction. *J Biomech*. 2014;47(5):1052–1059.

5. Meaney DF, Morrison B, Bass CD. The mechanics of traumatic brain injury: a review of what we know and what we need to know for reducing its societal burden. *J Biomech Eng*. 2014;136(2): 021008–021008–14. DOI: 10.1115/1.4026364

6. Shugar TA. *A Finite Element Head Injury Model*. Department of Transportation, National Highway Traffic Safety Administration. Port Hueneme, California; 1977.

7. Ward C, Chan M, Nahum A. Intracranial pressure–a brain injury criterion. Tech rep.; 1980.

8. Hosey RR, Liu YK. A homeomorphic finite element model of the human head and neck. In Callagher RH, Simon BR, Johnson TC, Gross JF , eds. *Finite Elements in Biomechanics*. Chapter 18, John Wiley & Sons, Ltd.; 1982:379–401.

9. Ruan J, Khalil T, King A. Human head dynamic response to side impact by finite element modeling. *J Biomech Eng*. 1991;113(3):276–283.

10. Mendis K. Finite element modeling of the brain to establish diffuse axonal injury criteria, The Ohio State University, 1992.

11. Bandak FA, Vorst MV, Stuhmiller LM, Mlakar PF, Chilton WE, Stuhmiller JH. An imaging-based computational and experimental study of skull fracture: finite element model development. *J of Neurotrauma*. 1995;12(4):679–688.

12. Kang H-S, Willinger R, Diaw BM, Chinn B. Validation of a 3D anatomic human head model and replication of head impact in motorcycle accident by finite element modeling. *Proceedings: Stapp Car Crash Conference*, Lake Buena Vista, FL Vol. 41: Society of Automotive Engineers SAE; 1997. 329–338.

13. Al-Bsharat AS, Hardy WN, Yang KH, Khalil TB, Tashman S, King AI. Brain/skull relative displacement magnitude due to blunt head impact: new experimental data and model. Tech. rep. SAE Technical Paper; 1999.

14. Zhang L, Yang KH, King AI. Comparison of brain responses between frontal and lateral impacts by finite element modeling. *J of Neurotrauma*. 2001;18(1):21–30.

15. Kleiven S, Hardy WN. Correlation of an FE model of the human head with local brain motion: consequences for injury prediction. *Stapp Car Crash Journal*. 2002;46:123–144.

16. Brands D, Bovendeerd P, Peters G, Wismans J. Predicting brain mechanics during closed head impact. *Technische Universiteit Eindhoven*, Eindhoven, The Netherlands; 2002.

17. Takhounts EG, Eppinger RH, Campbell JQ, Tannous RE. et al. On the development of the SIMon finite element head model. *Stapp Car Crash Journal*. 2003;47:107–133.

18. Horgan TJ. A finite element model of the human head for use in the study of pedestrian accidents, University College Dublin, 2005.

19. Kleiven S. Predictors for traumatic brain injuries evaluated through accident reconstructions. *Stapp Car Crash J*. 2007;51:81–114.

20. Iwamoto M, Nakahira Y, Tamura A, Kimpara H, Watanabe I, Miki K. Development of advanced human models in THUMS. *Proc. 6th European LS-DYNA Users' Conference*, Gothenburg 2007:47–56.

21. Takhounts EG, Ridella SA, Hasija V, Tannous RE, Campbell JQ, Malone D, Danelson K, Stitzel J, Rowson S, Duma S. Investigation of traumatic brain injuries using the next generation of simulated injury monitor (SIMon) finite element head model. *Stapp Car Crash Journal*. 2008;52:1–31.

22. Panzer MB, Myers BS, Capehart BP, Bass CR. Development of a finite element model for blast brain injury and the effects of CSF cavitation. *Ann Biomed Eng*. 2012;40(7):1530–1544.

23. Mao H, Zhang L, Jiang B, Genthikatti VV, Jin X, Zhu F, Makwana R, Gill A, Jandir G, Singh A. et al. Development of a finite element human head model partially validated with thirty five experimental cases. *J Biomech Eng*. 2013;135(11):111002–111002–15.

24. Tse KM, Tan LB, Lee SJ, Lim SP, Lee HP. Development and validation of two subject-specific finite element models of human head against three cadaveric experiments. *Int. J Numer Methods Biomed Eng*. 2014;30(3):397–415.

25. Cotton R, Pearce CW, Young PG, Kota N, Leung A, Bagchi A, Qidwai S. Development of a geometrically accurate and adaptable finite element head model for impact simulation: the Naval Research Laboratory–Simpleware Head Model. *Comput Meth Biomech Biomed Eng*. 2016;19(1):101–113.

26. Chatelin S, Deck C, Renard F, Kremer S, Heinrich C, Armspach J-P, Willinger R. Computation of axonal elongation in head trauma finite element simulation. *J Mech Behav Biomed Mater*. 2011;4(8):1905–1919.

27. Colgan NC, Gilchrist MD, Curran KM. Applying DTI white matter orientations to finite element head models to examine diffuse TBI under high rotational accelerations. *Prog Biophys Mol Biol*. 2010;103(2):304–309.

28. Wright RM, Ramesh K. An axonal strain injury criterion for traumatic brain injury. *Biomech Model Mechanobiol*. 2012;11(1-2):245–260.

29. Wright RM, Post A, Hoshizaki B, Ramesh KT. A multiscale computational approach to estimating axonal damage under inertial loading of the head. *J of Neurotrauma*. 2013;30(2):102–118.

30. Kraft RH, Mckee PJ, Dagro AM, Grafton ST. Combining the finite element method with structural connectome-based analysis for modeling neurotrauma: connectome neurotrauma mechanics. *PLOS Comput Biol*. 2012;8(8):e1002619. DOI: 10.1371/journal.pcbi.1002619

31. Sahoo D, Deck C, Willinger R. Development and validation of an advanced anisotropic visco-hyperelastic human brain FE model. *J Mech Behav Biomed Mater*. 2014;33: 24–42.

32. Giordano C, Kleiven S. Connecting fractional anisotropy from medical images with mechanical anisotropy of a hyperviscoelastic fibre-reinforced constitutive model for brain tissue. *J R Soc Interface* . 2014;11(91):20130914. DOI: 10.1098/rsif.2013.0914

33. Giordano C, Kleiven S. Evaluation of axonal strain as a predictor for mild traumatic brain injuries using finite element modeling. *Stapp Car Crash Journal*. 2014;58:29–61.

34. Ji S, Zhao W, Ford JC, Beckwith JG, Bolander RP, Greenwald RM, Flashman LA, Paulsen KD, McAllister TW. Group-wise evaluation and comparison of white matter fiber strain and maximum principal strain in sports-related concussion. *J of Neurotrauma*. 2015;32(7):441–454.

35. Zhao W, Ford JC, Flashman LA, McAllister T, Ji S. White matter injury susceptibility via fiber strain evaluation using whole-brain tractography. *J of Neurotrauma*. 2016. DOI: 10.1089/neu.2015.4239

36. Zhang L, Lake S, Barocas V, Shephard M, Picu R. Cross-linked fiber network embedded in an elastic matrix. *Soft Matter*. 2013;9(28):6398–6405.

37. Ortiz M, Leroy Y, Needleman A. A finite element method for localized failure analysis. *Comput Meth Appl Mech Eng*. 1987;61(2):189–214.

38. Belytschko T, Fish J, Engelmann BE. A finite element with embedded localization zones. *Comput Meth Appl Mech Eng*. 1988;70(1):59–89.

39. Fish J, Belytschko T. Elements with embedded localization zones for large deformation problems. *Comput Struct*. 1988;30(1): 247–256.

40. Phillips D, Zienkiewicz O. Finite element non-linear analysis of concrete structures. *Institution of Civil Engineers, Proceedings*, vol. 61; 1976. DOI: http://dx.doi.org/10.1680/iicep.1976.3503

41. Elwi A-EA, Murray DDW, University of Alberta. Dept. of Civil Engineering. Nonlinear analysis of axisymmetric reinforced concrete structures. *PhD thesis*, University of Alberta, 1981.

42. Tabatabaei S, Lomov SV, Verpoest I. Assessment of embedded element technique in meso-FE modelling of fibre reinforced composites. *Compos Struct*. 2014;107:436–446.

43. Korunović N, Trajanović M, Stojković M, Mišić D, Milovanović J. Finite element analysis of a tire steady rolling on the drum and comparison with experiment. *Strojniški vestnik-J Mech Eng*. 2011;57(12):888–897.

44. Tabatabaei S, Lomov SV. Eliminating the volume redundancy of embedded elements and yarn interpenetrations in meso-finite element modelling of textile composites. *Comput Struct*. 2015;152:142–154.

45. Lin S, Hapach LA, Reinhart-King C, Gu L. Towards tuning the mechanical properties of three-dimensional collagen scaffolds using a coupled fiber-matrix model. *Mater*. 2015;8(8):5376–5384.

46. Jiang WG, Hallett SR, Wisnom MR. Development of domain superposition technique for the modelling of woven fabric composites. *Mechanical response of composites*. Netherlands: Springer; 2008:281–291.

47. Iarve EV, Mollenhauer DH, Zhou EG, Breitzman T, Whitney TJ. Independent mesh method-based prediction of local and volume average fields in textile composites. *Composites Part A: Applied Science and Manufacturing*. 2009;40(12):1880–1890.

48. Wedeen VJ, Wang R, Schmahmann JD, Benner T, Tseng W, Dai G, Pandya D, Hagmann P, D'Arceuil H, de Crespigny AJ. Diffusion spectrum magnetic resonance imaging (DSI) tractography of crossing fibers. *Neuroimage*. 2008;41(4):1267–1277.

49. Mori S, Crain BJ, Chacko V, Van Zijl P. Three-dimensional tracking of axonal projections in the brain by magnetic resonance imaging. *Annals of Neurology*. 1999;45(2):265–269.

50. Bonilha L, Nesland T, Rorden C, Fillmore P, Ratnayake RP, Fridriksson J. Mapping remote subcortical ramifications of injury after ischemic strokes. *Behavioural Neurology*. 2014;2014. DOI: http://dx.doi.org/10.1155/2014/215380.

51. Rorden C. *dcm2nii DICOM to NIfTI Conversion*: The source for neuroimaging: MRIcoron; 2009.

52. Soares JM, Alves V, Sousa N, Marques PCG. A hitchhiker's guide to diffusion tensor imaging. In; 2013.

53. Liao W, Zhang Z, Pan Z, Mantini D, Ding J, Duan X, Luo C, Wang Z, Tan Q, Lu G. et al. Default mode network abnormalities in mesial temporal lobe epilepsy: a study combining fMRI and DTI. *Human Brain Mapping*. 2011;32(6):883–895.

54. Santillo AF, Mårtensson J, Lindberg O, Nilsson M, Manzouri A, Waldö ML, van Westen D, Wahlund L-O, Lätt J, Nilsson C. Diffusion tensor tractography versus volumetric imaging in the diagnosis of behavioral variant frontotemporal dementia. *PloS one*. 2013;8(7):e66932. DOI: 10.1371/journal.pone.0066932

55. Torgerson CM, Irimia A, Leow AD, Bartzokis G, Moody TD, Jennings RG, Alger JR, Van Horn JD, Altshuler LL. DTI tractography and white matter fiber tract characteristics in euthymic bipolar I patients and healthy control subjects. *Brain Imaging and Behavior*. 2013;7(2):129–139.

56. Guy J, Ellis E, Kelley K, Hope GM. Spectra of G ratio, myelin sheath thickness, and axon and fiber diameter in the guinea pig optic nerve. *Journal of Comparative Neurology*. 1989;287(4):446–454.

57. Balakrishnan S, Murray DW, Finite element prediction of reinforced concrete behavior (Structural Engineering Report no.: 138). Department of Civil Engineering, University of Alberta, 1986.

58. Hartl H, Handel C. 3D finite element modeling of reinforced concrete structures. *Graz Univ. of Technol., Inst. Of Structural Concrete*, Austria; 2000:1–10.

59. Hardy WN, Foster CD, Mason MJ, Yang KH, King AI, Tashman S. Investigation of head injury mechanisms using neutral density technology and high-speed biplanar x-ray.*Stapp Car Crash Journal*. 2001;45:337–368.

60. Hardy WN, Mason MJ, Foster CD, Shah CS, Kopacz JM, Yang KH, King AI, Bishop J, Bey M, Anderst W. A study of the response of the human cadaver head to impact. *Stapp Car Crash Journal*. 2007;51:17–80.

61. Itoh S, Hamashima H, Murata K, Kato Y. Determination of JWL parameters from underwater explosion test. *12th International Detonation Symposium*: Citeseer; 2002:0.

62. Wittek A, Omori K. Parametric study of effects of brain-skull boundary conditions and brain material properties on responses of simplified finite element brain model under angular acceleration impulse in sagittal plane. *JSME Int J, Ser C*. 2003;46(4):1388–1399.

63. Chafi MS, Ganpule S, Gu L, Chandra N. Dynamic response of brain subjected to blast loadings: influence of frequency ranges. *Int Appl Mech*. 2011;3(04):803–823.

64. Chatelin S, Deck C, Willinger R. An anisotropic viscous hyperelastic constitutive law for brain material finite-element modeling. *J Biorheol*. 2013;27(1-2):26–37.

65. Shuck L, Advani S. Rheological response of human brain tissue in shear. *J of Basic Eng*. 1972;94(4):905–911.

66. Nahum AM, Smith R, Ward CC. Intracranial pressure dynamics during head impact. Tech. rep. SAE technical paper; 1977.

67. Yao J, Yang J, Otte D. Investigation of head injuries by reconstructions of real-world vehicle-versus-adult-pedestrian accidents. *Saf Sci*. 2008;46(7):1103–1114.

68. Margulies SS, Thibault LE. A proposed tolerance criterion for diffuse axonal injury in man. *J Biomech*. 1992;25(8):917–923.

69. Bain AC, Meaney DF. Tissue-level thresholds for axonal damage in an experimental model of central nervous system white matter injury. *J Biomech Eng*. 2000;122(6):615–622.

70. Morrison III B, Saatman KE, Meaney DF, Mcintosh TK. In vitro central nervous system models of mechanically induced trauma: a review. *J Neurotrauma*. 1998;15(11):911–928.

71. Morrison III B, Cullen DK, LaPlaca M. In vitro models for biomechanical studies of neural tissues. *Neural Tissue Biomech*. Berlin Heidelberg: Springer, 2011:247–285.

72. Deck C, Willinger R. Improved head injury criteria based on head FE model. *Int J Crashworthiness*. 2008;13(6):667–678.

73. Garimella HT, Yuan H, Johnson BD, Slobounov SL, Kraft RH. A two-fiber anisotropic constitutive model of human brain with intravoxel heterogeneity of fiber orientation using diffusion spectrum imaging (DSI). *ASME 2014 International Mechanical Engineering Congress and Exposition*. Montreal, Canada: American Society of Mechanical Engineers; 2014.

74. Mao H, Gao H, Cao L, Genthikatti VV, Yang KH. Development of high-quality hexahedral human brain meshes using feature-based multi-block approach. *Comput Meth Biomech Biomed Eng*. 2013;16(3):271–279.

75. Gennarelli TA, Thibault LE, Adams JH, Graham DI, Thompson CJ, Marcincin RP. Diffuse axonal injury and traumatic coma in the primate. *Ann of Neurology*. 1982;12(6):564–574.

76. Gennarelli TA, Tomei G, Wiser R, Graham D, Adams J. Directional dependence of axonal brain injury due to centroidal and non-centroidal acceleration. Tech. rep. SAE technical paper; 1987.

77. Fish J. The s-version of the finite element method. *Comput Struct*. 1992;43(3):539–547.

78. Begonia M, Prabhu R, Liao J, Whittington W, Claude A, Willeford B, Wardlaw J, Wu R, Zhang S, Williams L. Quantitative analysis of brain microstructure following mild blunt and blast trauma. *J Biomech*. 2014;47(15):3704–3711.

79. Motiwale S, Eppler W, Holligsworth D, Hollingsworth C, Morgenthau J, Kraft RH. Application of neural networks for filtering non-impact transients recorded from biomechanical sensors. *Proceedings of IEEE International Conference on Biomedical and Health Informatics*. Las Vegas, NV: IEEE; 2016.

80. Monson KL, Barbaro NM, Manley GT. Biaxial response of passive human cerebral arteries. *Ann Biomed Eng*. 2008;36(12): 2028–2041.

APPENDIX

A. Definitions of quality metrics

The following definitions are taken from ANSYS ICEMCFD 14.5.7 help manual.

Quality: The quality is a weighted diagnostic between Determinant (between -1 and 1), Max Orthogls (this calculates the maximum deviation of internal angles of the elements from 90 degrees; normalized between -1 and 1; if deviation from orthogonality is greater than 90 degrees, then the normalized value will be smaller than 0), and Max Warpgls (maximum warp of quad faces of the element; normalized between 0 and 1; warpage of 0 degrees is 1, warpage of 180 degrees is 0). The minimum of the 3 normalized diagnostics will be used.

Determinant: The Determinant, more properly defined as the relative determinant, is the ratio of the smallest determinant of the jacobian matrix divided by the largest determinant of the jacobian matrix, where each determinant is computed at each node of the element. A Determinant value of 1 would indicate a perfectly regular mesh element, 0 would indicate an element degenerate in one or more edges, and negative values would indicate inverted elements.

Max angle: This calculates the maximum internal angle of quadfaces or trifaces of elements.

Min angle: This calculates the minimum internal angle of the quadfaces or trifaces of the elements.

Orthogonal quality: The orthogonal quality for cells is computed using the face normal vector, the vector from the cell centroid to the centroid of each of the adjacent cell, and the vector from the cell centroid to centroid of each of the faces.

The following quantities are computed for each face:

- The cosine of the angle between the face normal vector and the cell centroid to adjacent cell centroid vector.
- The cosine of the angle between the face normal vector and the cell centroid to face center vector.

The minimum value obtained from calculating these quantities for all the faces is defined as the orthogonal quality of the cell. The worst cells will have an orthogonal quality close to 0 while the best cells will have an orthogonal quality close to 1.

Skew: Skewness is defined as the normalized worst angle between each of the 6 face normals and the vector defined by the centroid of the hexahedron and the center of face.

B. Center of mass accelerations for different loading conditions

Figures B.1 and B.2 show the center of mass accelerations under different loading conditions used in this paper.

C. Axonal fiber bundles−beam elements vs truss elements:

Material properties: The ABAQUS does not allow hyperelastic beam elements in ABAQUS Explicit. Therefore, we used elastic beam elements to describe axonal fiber bundles. The elastic material properties for the bundles were derived from the small strain behavior of hyperelastic stress-strain curve, i.e., young's modulus for the bundles is derived from the slope of the stress-strain curve at zero strain. The material properties used in these simulations are listed below in Table C.1.

Input loading conditions: The model is subjected to the loading conditions same as that of Ji et al[34] as shown in Figure B.2 (same as that of the model with truss
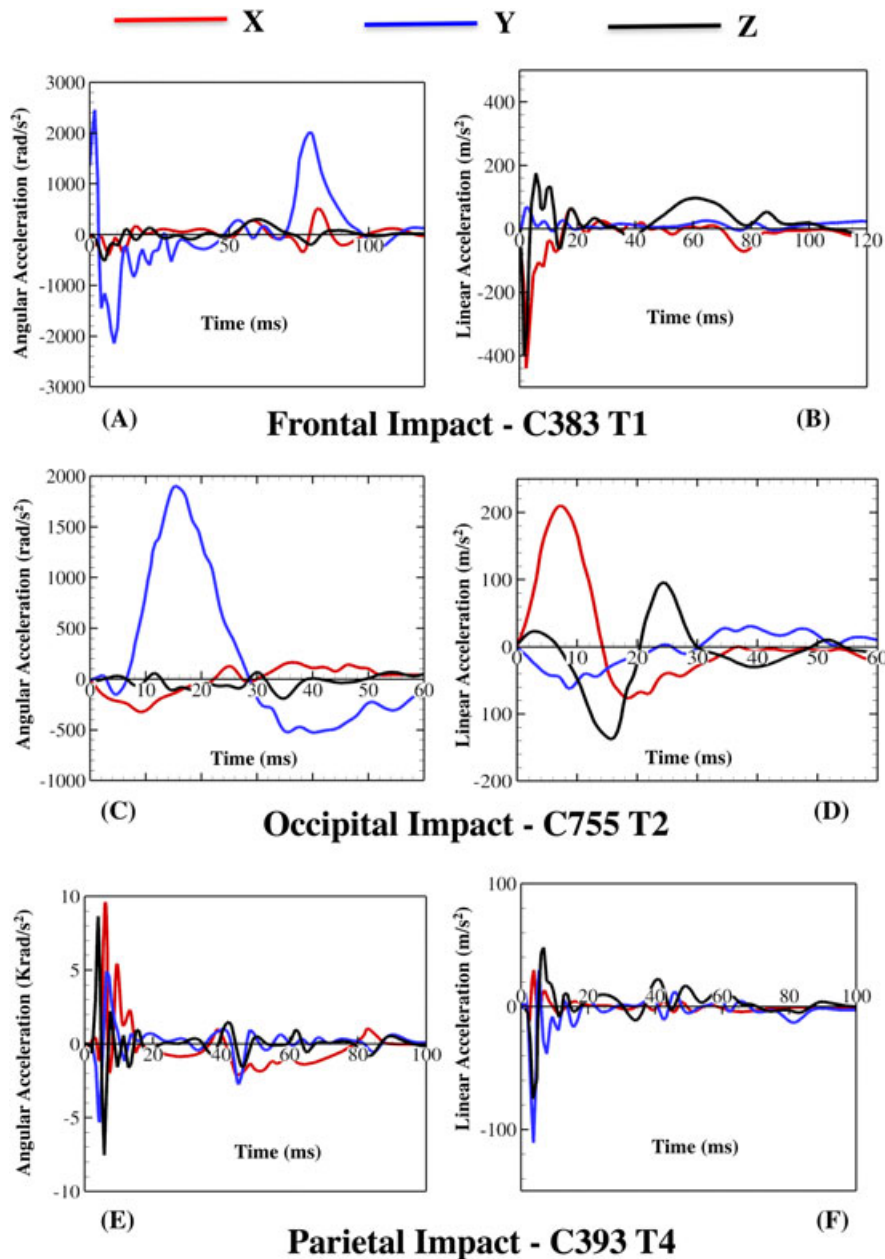
FIGURE B.1 Input accelerations from Hardy et al[59,60] displacement validation experiments for Frontal (C383T1), Occipital (C755T2), and Parietal (C393T4) loading conditions. The legend at the top applies for all the figures
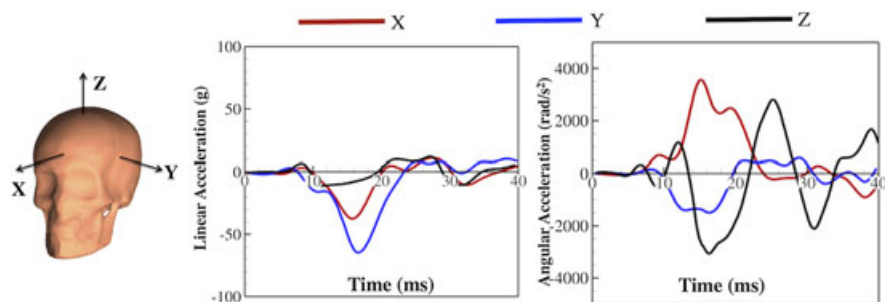
FIGURE B.2 Input acceleration curves for the injury criterion comparison in results section. This loading scenario corresponds to the Case 9218 (caused concussion in high school football player) from the work of Ji et al[34]

elements). The accelerations were applied to the center of mass of the head model.

Results: Figure C.1A-C shows the comparison of maximum strain, mean strain, and the percentage of

damaged elements respectively for both the models (i.e., model with beam elements and model with truss elements). A peak strain of 0.4052 was observed in the model with beam elements whereas a peak strain of 0.3871 was observed in the model with truss elements. Similarly a peak average strain of 0.0190 was observed in the model with beam elements compared to 0.0163 in the model with truss elements. A cumulative damage (percentage of damaged elements) of 3.9% was observed in the model with beam elements compared to the 1.8% damage in the model with truss elements. Figure C.1D shows the maximum shear strain observed in both the models. A peak shear strain of 0.3981 was observed in the model with beam elements whereas no shear strains were observed in the model with truss elements.

Discussion: Above results show that peak strains (maximum and average) observed in case of beam elements are only slightly higher than that of the model with truss elements. At the same time, percentage of damaged beam elements (3.9%) is almost double that of the damaged truss elements (1.8%). This might be due to the combined effect of inclusion of bending strains as well as the use of elastic material to describe the beam elements. Even though inclusion of bending effects might improve the accuracy of the model, inclusion of elastic properties might overemphasize the extent of injury (as observed from the percentage of damaged

TABLE C.1 Table showing different anatomic components, material models and corresponding material parameters used in the finite element model

Anatomical Components	Material Model	Material Parameters	References
Axonal fibers	Elastic	$\rho = 1040$ kg/m^3	64
		$E = 63.3$ kPa	
		$\nu = 0.5$	

elements). The low average strain observed might be due to the inclusion of compressive strains while calculating averages. Besides the above results, shear strains were also observed in the model with beam elements (not observed when truss elements are used). This is due to the resistance of beam elements to bending loads. This information could enable us to look into a new injury mechanism, i.e., shear damage of axonal bundles. Although a peak shear strain of 0.3941 was observed in the model, the average strain observed was very less (peak average strain observed = 0.0001). These preliminary observations indicate that only a few axonal fiber bundles are prone to shear damage. This is an interesting observation, and this line of research could be very helpful in studying the mechanical behavior of individual axonal fiber tracts for a particular loading condition. A detailed study of shear strains in axonal fiber bundles will be included in our future work.
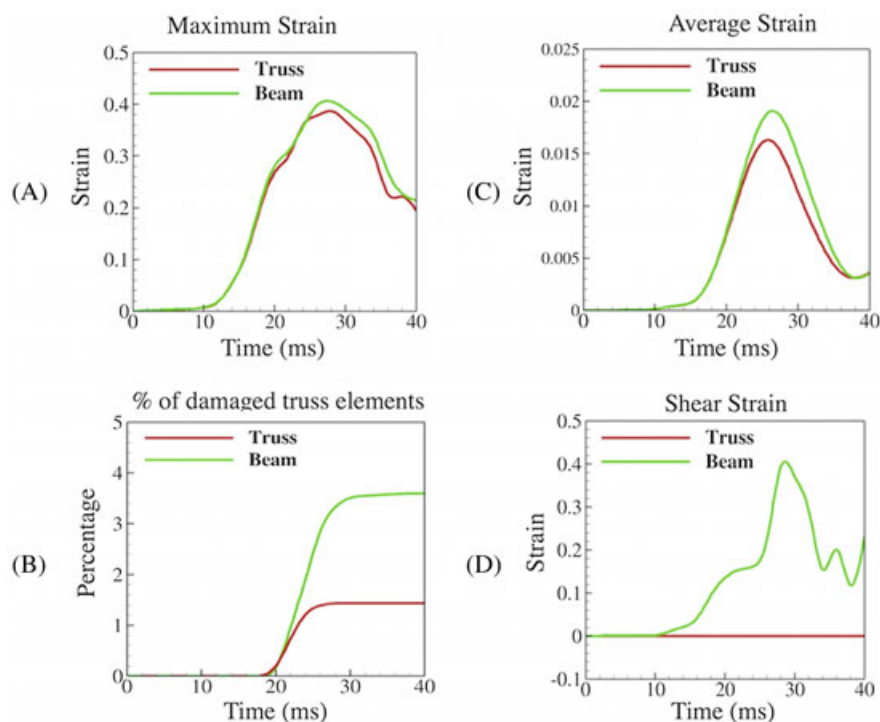
FIGURE C.1 Comparison of maximum strain during an applied impact loading between model with beam elements and model with truss elements